Nucl. Fusion **52** (2012) 013014 (25pp) doi:10.1088/0029-5515/52/1/013014

Investigation of a transient energetic charge exchange flux enhancement ('spike-on-tail') observed in neutral-beam-heated H-mode discharges in the National Spherical Torus Experiment

S.S. Medley[1], Ya.I. Kolesnichenko[2], Yu.V. Yakovenko[2], R.E. Bell[1], A. Bortolon[3], N.A. Crocker[4], D.S. Darrow[1], A. Diallo[1], C.W. Domier[5], R.J. Fonck[6], E.D. Fredrickson[1], S.P. Gerhardt[1], N.N. Gorelenkov[1], G.J. Kramer[1], S. Kubota[4], B.P. LeBlanc[1], K.C. Lee[5], E. Mazzucato[1], G.R. McKee[6], M. Podestà[1], Y. Ren[1], A.L. Roquemore[1], D.R. Smith[6], D. Stutman[7], K. Tritz[7] and R.B. White[1]

[1] Princeton Plasma Physics Laboratory, Princeton, NJ 08543, USA[a]
[2] Institute for Nuclear Research, 03680, Kyiv, Ukraine
[3] University of California, Irvine, CA 90095, USA
[4] University of California, Los Angeles, CA 90095, USA
[5] Department of Applied Science, University of California, Davis, CA 95616, USA
[6] Department of Engineering Physics, University of Wisconsin-Madison, Madison, WI 53706, USA
[7] Johns Hopkins University, Baltimore, MD 21218, USA

E-mail: medley@pppl.gov

Received 14 June 2011, accepted for publication 22 November 2011
Published 23 December 2011
Online at stacks.iop.org/NF/52/013014

Abstract
In the National Spherical Torus Experiment (NSTX), a large increase in the charge exchange neutral flux localized around the neutral beam (NB) injection full energy is measured using a neutral particle analyser. Termed the high-energy feature (HEF), it appears on the NB-injected energetic-ion spectrum only in discharges where tearing or kink-type modes ($f < 50$ kHz) are absent, toroidal Alfvén eigenmode activity ($f \sim 50$–150 kHz) is weak and global Alfvén eigenmode (GAE) activity ($f \sim 400$–1000 kHz) is robust. Compressional Alfvén eigenmode activity ($f > 1000$ kHz) is usually sporadic or absent during the HEF event. The HEF exhibits growth times of $\Delta t \sim 20$–80 ms, durations spanning 100–600 ms and peak-to-base flux ratios up to $H = F_{\max}/F_{\min} \sim 10$. In infrequent cases, a slowing-down distribution below the HEF energy can develop that continues to evolve over periods of order 100 ms, a time scale long compared with the typical fast-ion equilibration times. HEFs are observed only in H-mode (not L-mode) discharges with injected power $P_b \geqslant 4$ MW and in the pitch range $\chi \equiv v_{||}/v \sim 0.7$–$0.9$; i.e. only for passing particles. Increases of order 10–30% in the measured neutron yield and total stored energy that are observed to coincide with the feature appear to be driven by concomitant broadening of measured $T_e(r)$, $T_i(r)$ and $n_e(r)$ profiles and not the HEF itself. While the HEF has minimal impact on plasma performance, it nevertheless poses a challenging wave–particle interaction phenomenon to understand. Candidate mechanisms for HEF formation are developed based on quasilinear (QL) theory of wave–particle interaction. The only mechanism found to lead to the large NPA flux ratios, $H = F_{\max}/F_{\min}$, observed in NSTX is the QL evolution of the energetic-ion distribution,

[a] Princeton Plasma Physics Laboratory Reports are available in PDF format at: http://www.pppl.gov/pub_report/

$F_b(E, \chi, r)$, in phase space. A concomitant loss of some particles is observed due to interaction through cyclotron resonance of the particles with destabilized modes having sufficiently high frequencies, $f \sim 700$–1000 kHz, in the plasma frame that are tentatively identified as GAEs.

1. Introduction

The National Spherical Torus Experiment (NSTX) [1, 2] provides an excellent platform for investigation of MHD-induced interactions driven by both low-frequency ($f < 50$ kHz) MHD modes such as neoclassical tearing modes (NTMs) and kink-type modes but especially for wave–particle interactions involving higher frequency ($50 < f$(kHz) < 2000) Alfvén eigenmodes. NSTX is a midsize low aspect ratio fusion research facility with auxiliary heating from neutral beam injection (NBI) and high harmonic fast wave (HHFW) launch. Typical NSTX parameters are major radius $R_o = 0.85$–0.9 m, minor radius $a = 0.67$ m resulting in an aspect ratio of $A = R_o/a \sim 1.3$, plasma current $I_p = 0.3$–1.5 MA and toroidal field $B_T = 0.35$–0.55 T. Three co-directed deuterium neutral beam (NB) sources have injected power up to $P_b = 7$ MW at full neutral energies up to $E_b = 100$ keV. HHFW heating at 30 MHz is capable of delivering up to $P_{RF} \sim 6$ MW to deuterium and helium plasmas. The performance milestones that were achieved to date in NSTX have been reported elsewhere [3, 4, and references therein]. H-modes triggered by NBI heating are routinely obtained in NSTX and have become a standard operational scenario [5]. L–H transitions triggered by NBI heating have been obtained over a wide parameter range in $I_p \leqslant 1.2$ MA, $B_T \leqslant 5.5$ kG and $n_e \leqslant 8 \times 10^{13}$ cm^{-3} in either lower-single-null or double-null diverted discharges with elongation $\kappa \leqslant 2.6$, triangularity $\delta \leqslant 0.85$ and plasma pulse length exceeding 1.5 s.

A wide variety of fast-ion-driven instabilities are excited during high-power NBI in NSTX. Such beam-driven Alfvén eigenmodes [6–9] are destabilized when the fast-ion velocity v_b is larger than the Alfvén speed v_A. The modes can be divided into three categories; chirping energetic particle modes (EPM) in the frequency range 0–120 kHz, the toroidal Alfvén eigenmodes (TAEs) with a frequency range 50–200 kHz and the global and compressional Alfvén eigenmodes (GAE and CAE, respectively) between 300 kHz and the ion cyclotron frequency. The TAEs can appear either as saturated modes or as bursting modes. The bursting TAEs observed in NSTX [10–12] can cause significant fast-ion losses. In addition to Alfvénic modes, energetic-ion redistribution and/or loss associated with low-frequency NTM or kink-type MHD activity has been observed in many fusion experiments, for example, NSTX [13, 14] and ASDEX-U [15, 16].

If MHD-induced energetic-ion redistribution is sufficiently severe then ion loss to the NSTX first-wall structures can occur in addition to bad-orbit driven prompt loss to the walls. The prompt loss of NB ions from NSTX is expected to be between 12% and 42% of the total beam power [17]. Such losses are diagnosed, for example, by Faraday cup [18] and scintillator fast loss ion probe (sFLIP) [19] diagnostics that detect ions on loss orbits. Resonant interaction of high-energy particles with magnetic perturbations in toroidal devices can produce large-scale modification of the particle distribution, sometimes leading to particle loss. Spherical tokamaks, including NSTX [20–23], START [24] and MAST [25, 26], are particularly susceptible to fast-ion-driven instabilities due primarily to their relatively low toroidal field but also in some instances due to the direct effect of the low aspect ratio.

In quiescent or MHD benign NSTX discharges, neutral particle analyser (NPA) measurements of the energetic beam ion distribution are consistent with classical behaviour [27]. However, the appearance of MHD activity can have a pronounced effect on 'energetic' ($E \sim 10$–100 keV) ion populations in NSTX. Previous work using the $E \| B$ NPA diagnostic has dealt with MHD-induced energetic-ion redistribution associated with relatively low-frequency ($f < 100$ kHz) activity such as kink or tearing modes and TAE in NSTX [13, 28, 29]. In this work, the low-frequency activity is 'quiescent' and wave–particle interactions that affect the fast-ion distribution in physical and phase-space are driven by high-frequency ($400 < f < 1200$ kHz) Alfvén eigenmodes such as GAE and CAE.

The paper is organized as follows. Section 2 presents information on the key diagnostics used to measure MHD activity and energetic-ion distributions on NSTX. Section 3 introduces the high-energy feature (HEF) that is the core physics concept in this paper followed by examples of a 'transient' HEF in section 3.1 and a 'dual-energy' HEF in section 3.2. Available measurements of the Alfvén eigenmode radial structure associated with the HEF drive are given in section 4 and an overview of the parametric dependences of the HEF is given in section 5 including observations not documented in this paper due to space constraints. Section 6 presents TRANSP code analysis providing insight into the evolution of plasma parameters attending the HEF. Theoretical mechanisms for explaining the HEF phenomenon are given in section 7. The paper concludes in section 8 with a discussion and summary.

2. Diagnostics for investigation of wave–particle effects on energetic ions in NSTX

On NSTX, the frequency evolution and amplitude of Alfvén modes are measured using a suite of diagnostics including Mirnov magnetic coils, beam emission spectrometry (BES) [30], multichannel reflectometry [31], tangential collective high-k scattering [32], far-infrared tangential interferometery/polarimetry (FIReTIP) [33] and ultra-soft x-ray (USXR) [34] diagnostics. The neutron production in NSTX is predominantly from beam–target reactions and thus is a robust measure of the energetic-ion behaviour. Neutron data along with NPA and sFLIP diagnostics are used to assess fast-ion redistribution or loss due to MHD-induced effects. Diagnostics for measurement of the spatial structure of MHD activity in NSTX discharges are limited with BES and reflectometry being the most effective.

Energetic-ion energy distributions are usually measured using charge exchange neutral particle diagnostics [35]. The NPA on NSTX [36] utilizes a $E \| B$ (superimposed parallel electric and magnetic fields) spectrometer developed at the

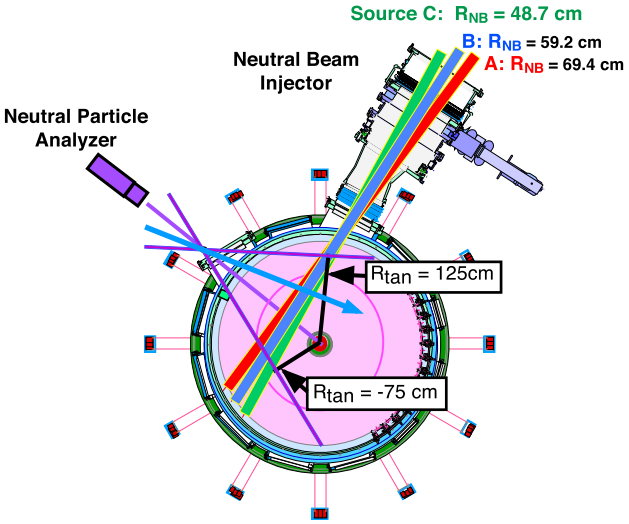

Figure 1. The NPA on NSTX views across the three NBI sources and can be scanned horizontally over a wide range of sightline tangency radii, R_{tan}, on a shot-to-shot basis. R_{tan}, is the perpendicular distance between the machine centre and the NPA sightline.

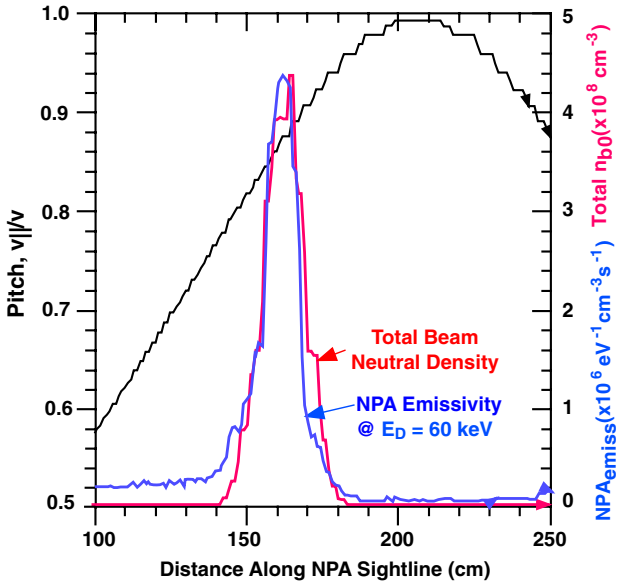

Figure 2. Emissivity and pitch-angle localization of the NPA flux arises from the intersection of the diagnostic sightline with the NB sources. The TRANSP-calculated emissivity includes beam primary and edge neutrals but not halo neutrals.

Princeton Plasma Physics Laboratory [37] that simultaneously measures the mass-resolved energy spectra of both H and D neutrals with a time resolution of ~1 ms set by signal-to-noise levels. A multi-anode microchannel plate detector provides up to 39 energy measurements for each of the H and D species. The calibrated energy range is $E = 0.5$–$150\,\mathrm{keV}$ and the energy resolution varies over a range of $\Delta E/E = 3$–7% from high to low energy.

As shown in figure 1, the NPA views across the co-injection paths of the three NBI sources on NSTX that inject at major tangency radii $R_{NB} = 69.4\,\mathrm{cm}$ (source A), $R_{NB} = 59.2\,\mathrm{cm}$ (source B) and $R_{NB} = 48.7\,\mathrm{cm}$ (source C). The NPA can be scanned horizontally over a wide range of tangency radii (as well as vertically) on a shot-to-shot basis. Figure 2 illustrates the core localization of the NPA flux in space and particle pitch, $v_\parallel/v$, that arises from the intersection of the diagnostic sightline with the primary neutral footprint (excluding halo neutrals) of the heating beams. (NPA edge emissivity is intentionally truncated by choice of the sightline origin.) This localization is strongest near the NBI full energy, but remains substantial over the entire slowing-down distribution. The spatial localization weakens at smaller NPA tangency radii, R_{tan}, due to attenuation of the beam neutral density with increasing penetration distance. For energetic ions having large orbits that make excursions near the plasma outer boundary, the role of the edge neutral density must be considered as well. In practice, this situation is complicated by lack of reliable measurements of the edge neutral density. However, limits on the role of the edge neutral density can be obtained using the TRANSP code simulator for the charge exchange neutral particle diagnostic on NSTX. For the NPA data presented in this paper, the analyser was fixed at $R_{tan} = 70\,\mathrm{cm}$ corresponding to an intersection with the NB footprint at $R_{maj} = 85\,\mathrm{cm}$ as depicted by the arrowed sightline in figure 1 although other data have been obtained for a tangency range of $R_{tan} = 55$–$90\,\mathrm{cm}$. For this setting, the core-weighted NPA measurements view energetic ions with pitch $v_\parallel/v \sim 0.8$–0.9 while measurements near the plasma periphery view pitch $v_\parallel/v \sim 0.5$–0.6.

3. Representative HEFs on energetic-ion spectra in NSTX

An increase in the NPA charge exchange flux that is localized at the NB full energy has been observed on NSTX that will be referred to as the 'high-energy feature' or HEF [38]. In the subsections below, examples are presented of HEFs that are classified according to selected dominant characteristics. To provide a reference for comparison with the representative discharges that exhibit HEF events, figure 3 shows NPA measurements for a typical H-mode discharge that is devoid of the HEF event. Panel (*a*) shows a typical NPA deuterium fast-ion spectrum characterized by energetic-ion depletion in the range $E_b/2 < E \leqslant E_b$. This depletion is driven by a combination of attenuation of injected beam neutrals and emerging charge exchange flux caused by rising electron density as well as potential MHD-induced energetic-ion redistribution or loss [13]. Panel (*b*) gives spectrum line-outs at $t = 200$, 350, 450 and 900 ms showing the progressive depletion of the spectra. Such NPA spectra are by far the most commonly observed in NSTX beam-heated H-mode discharges with the HEF occurring in $\leqslant 5\%$ of discharges.

HEFs have been observed over an extensive range of discharges during the 2009-10 NSTX campaigns. The HEF is observed only at the NB full injection energy, i.e. never at the NB fractional energies. The HEF exhibits rise-times of ~20–80 ms and durations up to hundreds of milliseconds and multiple HEFs can occur during a single discharge. Discharge conditions that appear to be simultaneously necessary (but not necessarily sufficient) for HEFs to occur are H-modes, $P_b \geqslant 4\,\mathrm{MW}$, no $n = 1, 2$ tearing or kink-like modes, reduced TAE activity and robust GAE activity.

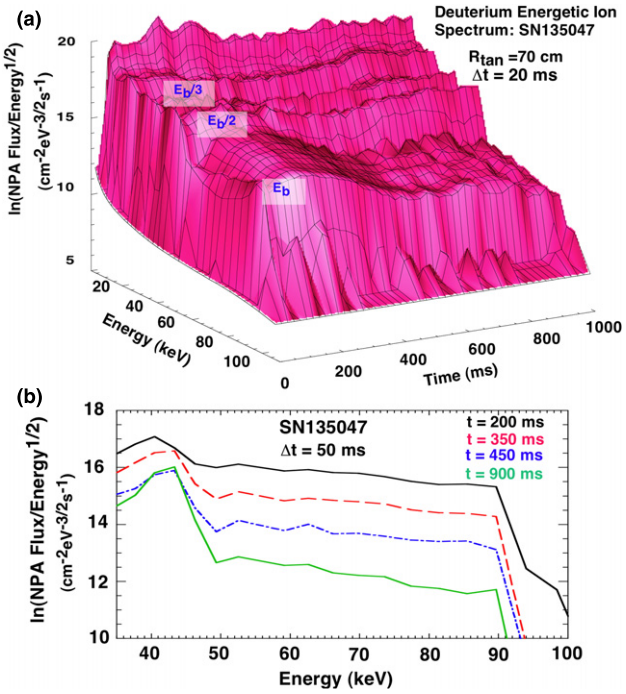

Figure 3. NPA energetic-ion measurements for SN135047 with the NB full, half and third injection energies indicated on the 3D distribution (*a*) and 2D energy spectra at selected times during the discharge (*b*).

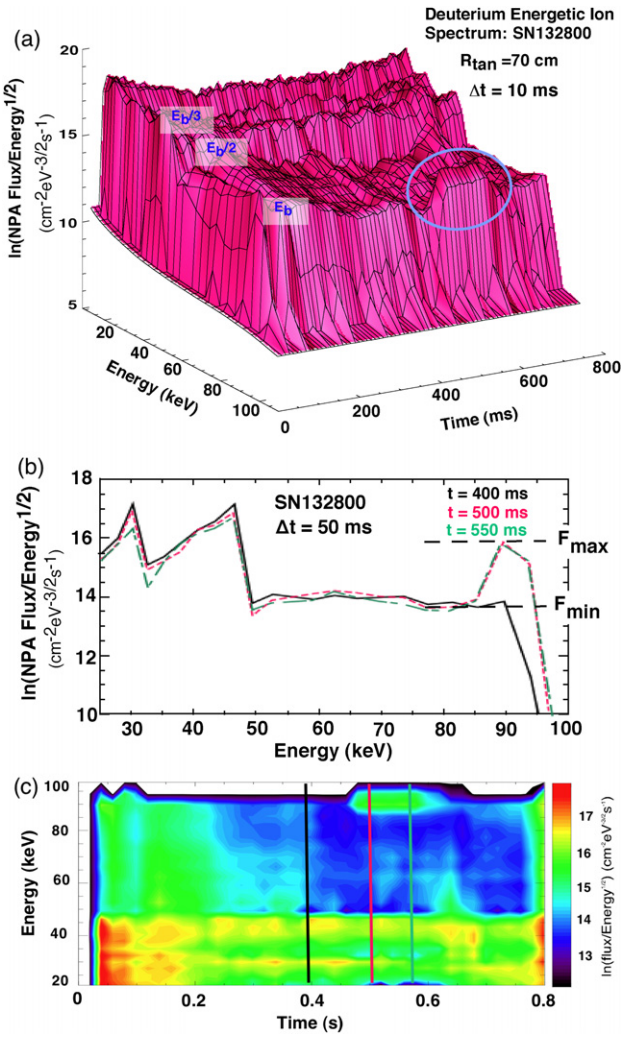

Figure 4. NPA energetic-ion measurements for SN132800 with the NB full, half and third injection energies indicated on the 3D distribution (*a*), 2D energy spectra at selected times during the discharge (*b*) and the flux contour plot (*c*).

HEFs can be categorized according to distinctive time evolution and energy characteristics [38]. A 'transient' HEF is characterized by being a single event with a duration in the range of $t \sim 100$–200 ms. An 'extended' HEF has a duration in the range of $t \sim 100$–600 ms. A 'persistent' HEF is characterized by the absence of a turn-on event and appears to evolve smoothly in time at the NB full energy following the initial NB injection phase and lasts throughout the duration of the plasma current flattop (up to 1000 ms). Also 'tandem' HEFs have been observed that are characterized by two or more events occurring sequentially in time during the same discharge. 'Dual-energy' HEFs have been observed in discharges with NB injection at two energies: e.g. $E_b = 90$ and 67 keV. In all HEF variations, the HEF on-periods coincide with intervals of reduced low-f MHD activity and robust GAE activity. Examples of 'transient' and 'dual-energy' HEFs are presented below.

3.1. 'Transient' HEF

A 'transient' HEF is characterized by being a single event with a duration in the range of $t \sim 100$–200 ms. A typical case is shown in figure 4(*a*) where the HEF occurs in the interval $t = 480$–600 ms identified by the blue circle on the NPA three-dimensional (3D) energetic-ion spectrum. From this and following panels, the HEF appears to abruptly *emerge above* the slowly varying flux level of the slowing-down distribution. Figure 4(*b*) shows individual spectra at $t = 400$, 500 and 550 ms. In order to characterize the strength of the HEF, it is useful to introduce the 'height' parameter $H = F_{max}/F_{min}$ where F_{max} and F_{min} are the flux at the peak and base of the HEF, respectively (note natural logarithmic ordinate). Although not shown, the height variation over the duration of the HEF is modest at $H = F_{max}/F_{min} \sim 8.9$–$11.0$ with the peak flux, F_{max}, remaining essentially constant and the change in height being caused by a decrease in the base flux, F_{min}. Panel (*c*) shows the NPA flux contour plot where the HEF is clearly evident by the transiently enhanced NPA flux at $E_b = 90$ keV ('spike-on-tail') at times demarked by the vertical red and green bands. From figure 4(*b*), it is evident that the HEF occurs at the NB full injection energy, $E_b = 90$ keV, and not at the NB fractional energies, $E_b/2 = 45$ keV and $E_b/3 = 30$ keV. Also notable is the absence of any slowing-down distribution evolving from the HEF energy. The spectrum was obtained for a NPA tangency radius of $R_{tan} = 70$ cm that localizes the measurement to the intersection with the NB footprint at a major radius of $R_m \sim 85$ cm.

Figure 5 shows Mirnov spectrograms for the GAE/CAE modes in the frequency range, $f = 400$–1200 kHz in panel (*a*) and for the NTM/TAE modes in the frequency range $f \leqslant 140$ kHz in panel (*b*) with injected NB power, P_b (MW),

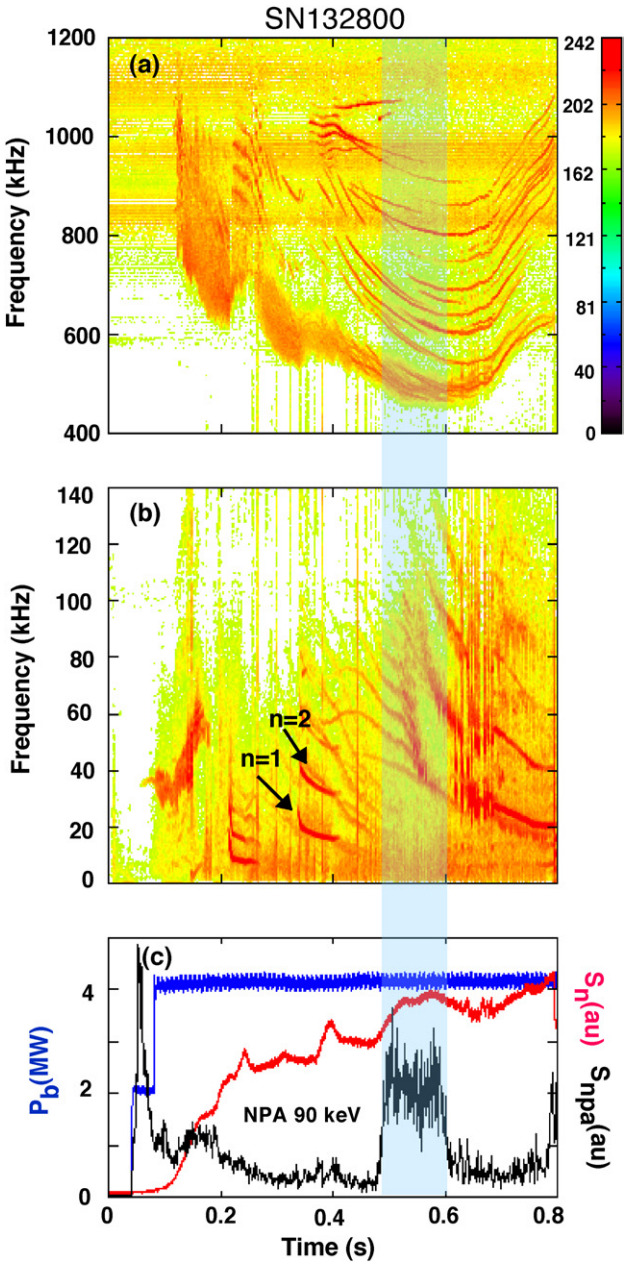

Figure 5. Mirnov spectrograms for SN132800 in the GAE/CAE (*a*) and the NTM/TAE (*b*) regimes plus waveforms showing the injected NB power, NPA signal at $E = 90$ keV and the volume neutron yield (*c*).

the NPA signal at $E_b = 90$ keV, S_{npa} (au) and total neutron yield, S_n (au) shown in panel (*c*). A vertical band demarks the HEF interval. This figure illustrates the MHD behaviour that is invariably correlated with the occurrence of the HEF. Referring to panel (*b*), HEF occurrence firstly requires that $f < 50$ kHz, $n = 1, 2$ NTM or kink-type modes be absent and the TAE activity be subdued.

Secondly, GAE activity must be robust as can be seen in panel (*a*). Furthermore, the GAE activity appears to be unaffected (i.e. is not modulated) by the HEF. Thirdly, the reappearance $n = 1, 2$ modes or strong TAE activity or bursting MHD (e.g. EPMs or TAE 'avalanches') terminates the HEF as seen in this case at $t > 600$ ms. Since the HEF and MHD activity are correlated, it is natural to assume that they are causally related. Figure 6 provides a collection of discharge and diagnostic data that is relevant to SN132800. The HEF interval is demarked with a shaded vertical band. Waveforms for plasma current, I_p (MA), injected NB power, P_b (MW), and line-averaged electron density, n_e ($\times 10^{13}$ cm^{-3}), are shown in panel (*a*). Panel (*b*) identifies high-frequency MHD for toroidal modes $n = 1$–8 obtained by fast Fourier transform analysis of the Mirnov spectrogram shown in panel (*f*) where a notable mode amplitude increase leads the onset of the HEF. No such correlation is observed for other bands in the high-frequency range. Panel (*c*) is the corresponding analysis for low-frequency toroidal modes $n = 1$–4 again showing that the HEF interval is devoid of low frequency $n = 1$, 2 NTM or kink-type activity and TAE activity is minimal. The δB_{rms} mode amplitude for the frequency range of 20–100 kHz is shown in panel (*g*) confirming a minimum in low-frequency mode activity during the HEF. Panel (*d*) shows the contour plot of the NPA flux versus energy. Panel (*e*) gives measured waveforms for neutron yield, S_n, total stored energy, W_T, and lower divertor D_α emission showing robust 'type 1' ELM activity during the HEF. The initial drop in D_α emission at $t \sim 0.16$ s marks the discharge transition to H-mode.

Figure 7 provides contour plots of multi-point Thomson scattering (MPTS) [39] measurements of electron temperature (*a*) and density (*c*) and charge exchange recombination spectroscopy (CHERS) [40] measurements of deuterium ion temperature (*b*), toroidal rotation velocity (*d*) and carbon impurity Z_{eff} (*e*) for SN132800. The HEF interval is marked with a shaded vertical band. With the onset of the HEF, the most pronounced change is an increase in the electron temperature from $T_e \sim 0.8$ keV to $T_e \sim 1.0$ keV over a broad core region of $70 < R(\text{cm}) < 130$. The core ion temperature remains relatively constant at $T_i \sim 1.2$ keV but the profile broadens with an increase from $T_i \sim 0.8$ keV to $T_i \sim 1.1$ keV in the outboard region $R \sim 120$–130 cm. The core electron density exhibits a modest ramp from $n_e \sim (8\text{–}9) \times 10^{13}$ cm^{-3}. The core toroidal velocity is relatively constant at $v_t \sim 220$ km s^{-1} and $Z_{eff} \sim 1.8 \pm 0.1$. Some correlations can be inferred between the noted changes in plasma profiles and in MHD activity in figures 5 and 6, but is not clear if the profile changes are caused by (or the cause of) the changes in MHD activity.

In figure 6(*e*), there appears to be a modest but distinct increase in the neutron yield, S_n, and total stored energy, W_T, during the HEF. However, this excursion lags the onset of the HEF and is attributed to the plasma profile changes noted in figure 7 and not the HEF itself. Further validation of this interpretation is provided by TRANSP code analysis presented in section 6.

3.2. 'Dual-energy' HEF

For discharges with NB sources A, B at $E_b = 90$ keV and C at $E_b = 67$ keV, HEFs have been observed at both NB full injection energies. The dual-energy HEFs sometimes over lap in time but most often they appear sequentially. A clean sequential case with relatively sharp turn-on and turn-off times is shown by the NPA 3D energetic-ion spectrum in figure 8(*a*)

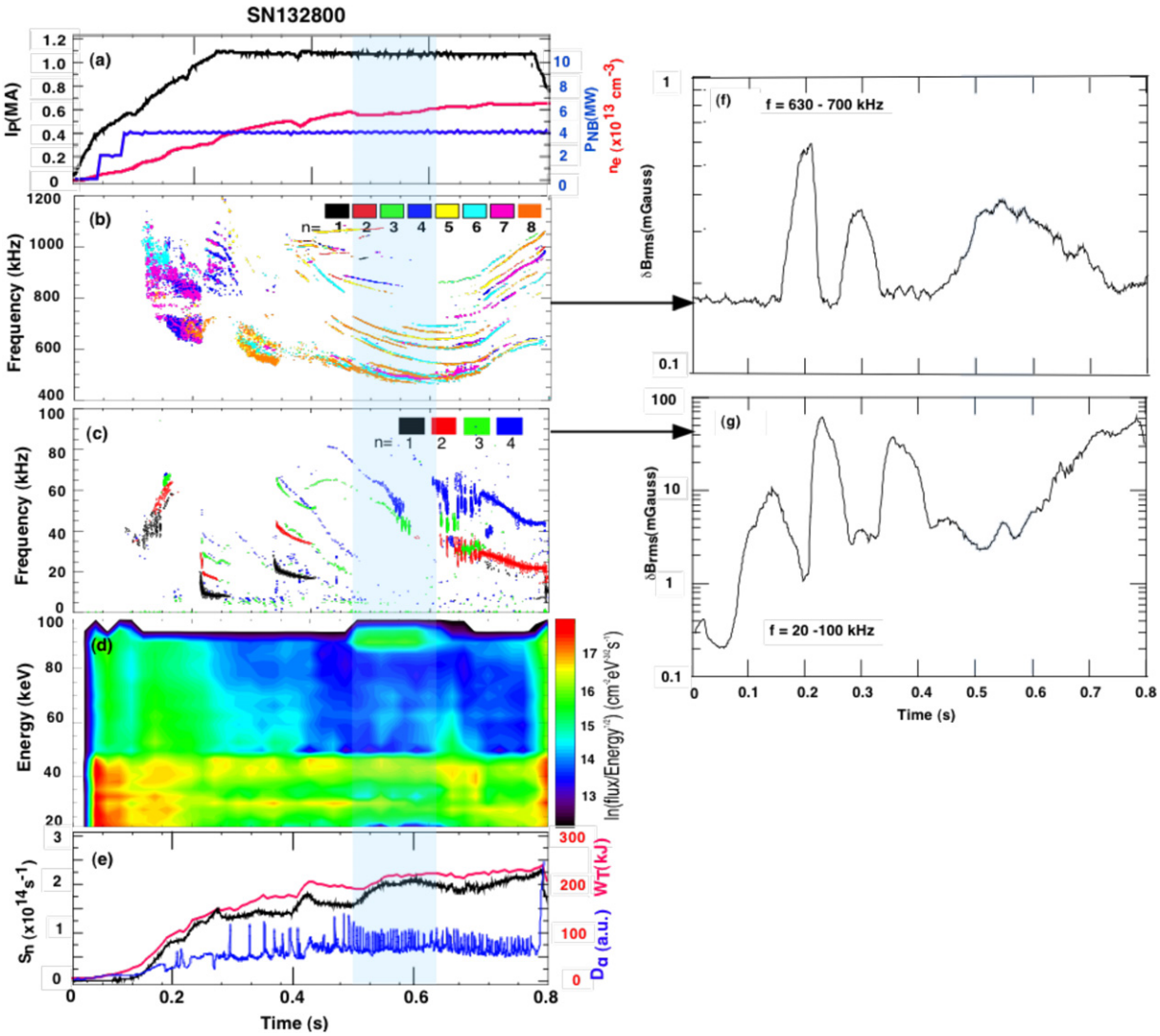

Figure 6. Selected plasma discharge data for SN132800: (*a*) plasma current, injected NB power and MPTS line-average electron density, (*b*) MHD mode analysis for the GAE/CAE regime, (*c*) MHD mode analysis for the NTM/TAE regime, (*d*) contour plot of the NPA energetic-ion spectrum and (*e*) volume neutron yield, total stored energy and D_α emission. Mirnov spectra $\delta B_{\rm rms}$ amplitude plots are shown for selected high (*f*) and low (*g*) frequency bands.

where the $E_{\rm b} = 90$ keV ('high' energy) HEF occurs first in the interval $t \sim 380$–670 ms (blue encircle) then turns off and is shortly followed by the $E_{\rm b} = 65$ keV ('low' energy) HEF in the interval $t \sim 680$–1000 ms (black encircle). An oscillatory HEF transition phase occurs in the period $t \sim 670$–680 ms as discussed momentarily. Figure 8(*b*) shows individual spectra at $t = 200$, 400 and 800 ms where the 'spike-on-tail' is clearly evident for both NB full injection energies. The height variation from onset to termination of the $E_{\rm b} = 90$ keV HEF is $H = F_{\rm max}/F_{\rm min} \sim 4.1 - 16.6$ (i.e. increases with time). The peak flux, $F_{\rm max}$, remains relatively constant with the change in height being caused by a decrease in the base flux, $F_{\rm min}$. For the $E_{\rm b} = 67$ keV HEF, the height variation from onset to termination is $H = F_{\rm max}/F_{\rm min} \sim 13.5$–$11.0$ (i.e. decreases with time). Again, the peak flux, $F_{\rm max}$, remains relatively constant with the change in height being caused in this case by an increase in the base flux, $F_{\rm min}$. Figure 8(*c*) shows the NPA flux contour plot where the high-energy HEF at $t = 400$ ms is demarked by a vertical red line and the low-energy HEF at $t = 800$ ms by a vertical black line. Dashed lines bracket the oscillatory transition phase.

Figure 9 shows Mirnov spectrograms for the GAE/CAE modes in the frequency range, $f = 400$–1200 kHz in panel (*a*) and for the NTM/TAE modes in the frequency range $f \leqslant 140$ kHz in panel (*b*) with injected NB power, $P_{\rm b}$ (MW), and total neutron yield, $S_{\rm n}$ (au) shown in panel (*c*). Also shown in panel (*c*) are the $S_{\rm npa}$ signals for the $E_{\rm b} = 90$ keV HEF (black curve demarked in time by a blue band) and for the $E_{\rm b} = 67$ keV HEF (green curve demarked in time by a green band). The gap between these bands brackets the oscillatory HEF transition phase. As seen in panel (*b*), the high-energy HEF occurs during a period that is devoid of $n = 1$, 2 kink or tearing-type modes and exhibits modest TAE activity. The transition to the low-energy HEF is marked by two strong EPM bursts/avalanches that collapse the high-energy HEF (and $S_{\rm n}$ as seen in panel (*c*)) while generating large spikes in the low-energy HEF. After two cycles the high-energy HEF remains suppressed while the low-energy HEF continues

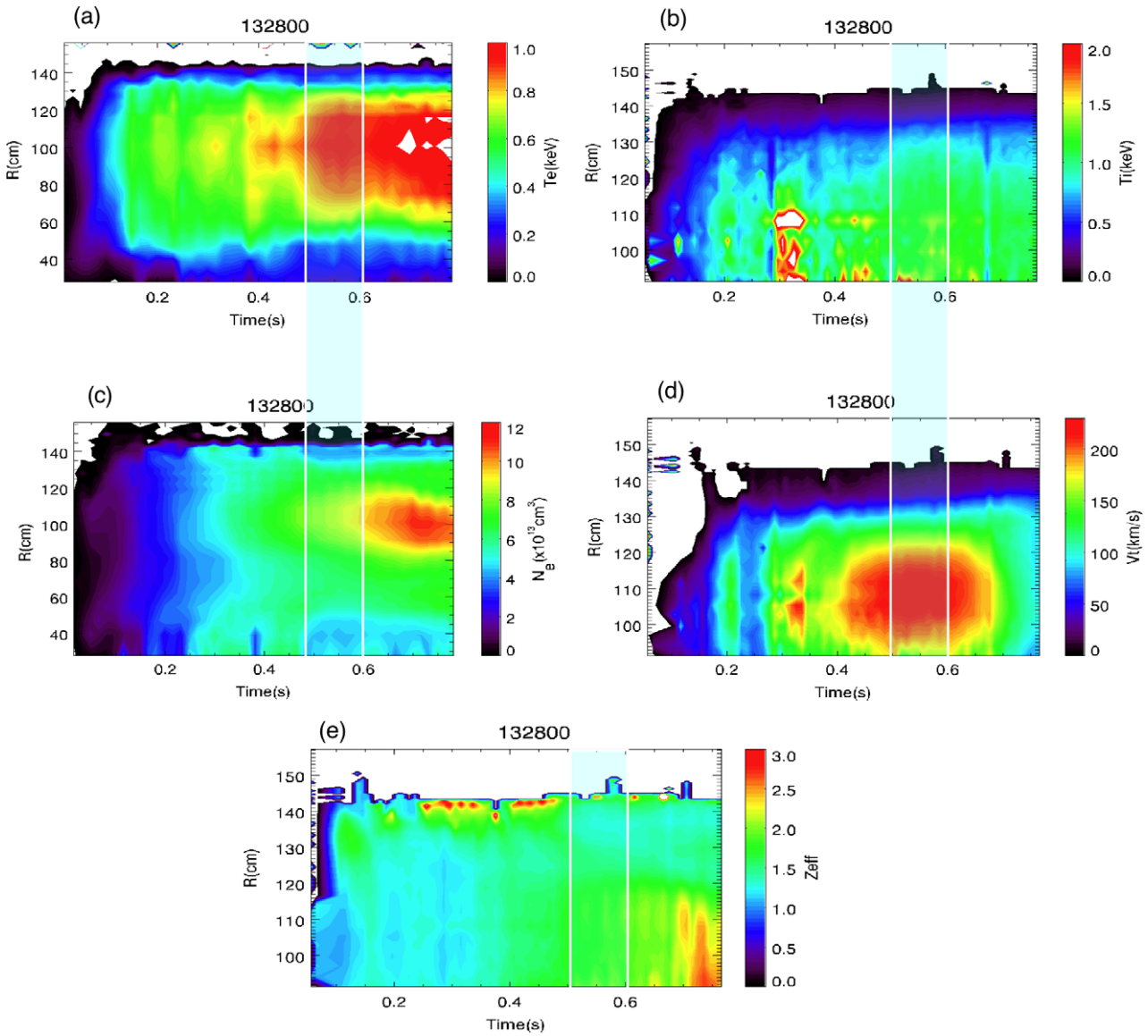

Figure 7. MPTS and CHERS contour plots for SN132800: (*a*) electron temperature, (*b*) deuterium ion temperature, (*c*) electron density, (*d*) toroidal rotation velocity and (*e*) carbon $Z_{\rm eff}$.

from $t \sim 680$–1000 ms. The remarkable point here is that the $E_{\rm b} = 67$ keV HEF exists in the presence of strong $n = 1, 2$ activity that always terminates the $E_{\rm b} = 90$ keV HEF.

Figure 10 shows a collection of discharge data that is relevant to SN135174 with shaded vertical bands demarking the times of interest as in the preceding figure. As seen in panels (*c*) and (*g*), the $E_{\rm b} = 90$ keV HEF interval is devoid of low frequency $n = 1$ NTM or kink-type modes and has only weak TAE activity while the inverse occurs during the $E_{\rm b} = 67$ keV HEF. Panels (*b*) and (*f*) show that a strong change in GAE/CAE activity that coincides with the transition between high and low-energy HEFs. An abrupt collapse in the toroidal rotation velocity, $v_{\rm t}$, occurs at this transition as can be seen in figure 11(*d*). Again the HEFs do not appear to drive any significant fluctuations or modulation of the GAE/CAE activity. Panel (*e*) shows sporadic ELM activity during both HEFs but possible changes in the neutron yield and total stored energy are obfuscated by preceding events.

Figure 11 provides contour plots of MPTS measurements of electron temperature (*a*) and density (*c*) and CHERS measurements of deuterium ion temperature (*b*), toroidal rotation velocity (*d*) and carbon impurity $Z_{\rm eff}$ (*e*) for SN135174 with the HEF intervals marked as before. With the onset of the $E_{\rm b} = 90$ keV HEF at $t \sim 0.38$ s, the electron temperature exhibits an abrupt increase from $T_{\rm e} \sim 0.6$ keV to $T_{\rm e} \sim 0.8$ keV over a broad core region of $80 < R({\rm cm}) < 120$. The core ion temperature increases from $T_{\rm i} \sim 0.8$ keV to $T_{\rm i} \sim 1.2 \pm 0.2$ keV with significant profile broadening in the region $R \sim 120$–135 cm. The core electron density exhibits a ramp from $n_{\rm e} \sim (6$–$8) \times 10^{13}$ cm^{-3}. The core toroidal rotation velocity increases from $v_{\rm t} \sim 180$ km s^{-1} to a relatively constant value of $v_{\rm t} \sim 220$ km s^{-1} and then collapses at the transition to the $E_{\rm b} = 67$ keV HEF. This rotation collapse drives the large change in GAE/CAE frequencies seen at the transition between high and low-energy HEFs in figures 9(*a*) and 10(*b*). During the $E_{\rm b} = 90$ keV HEF, the core carbon impurity remains

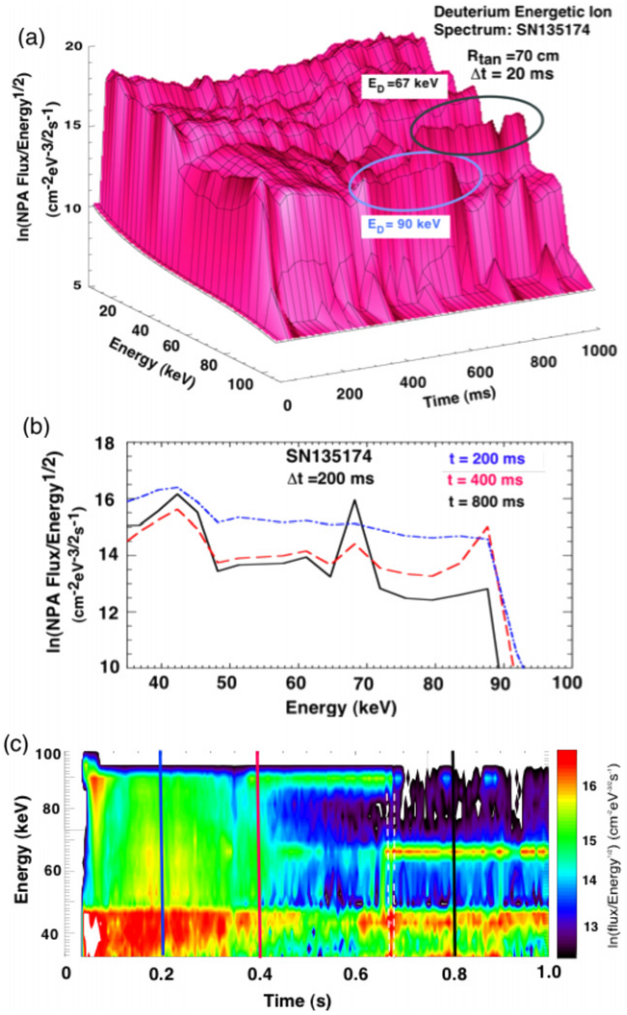

Figure 8. NPA energetic-ion measurements for SN135174 with the NB full, half and third injection energies indicated on the 3D distribution (*a*) and, 2D energy spectra at selected times during the discharge (*b*) and the flux contour plot (*c*).

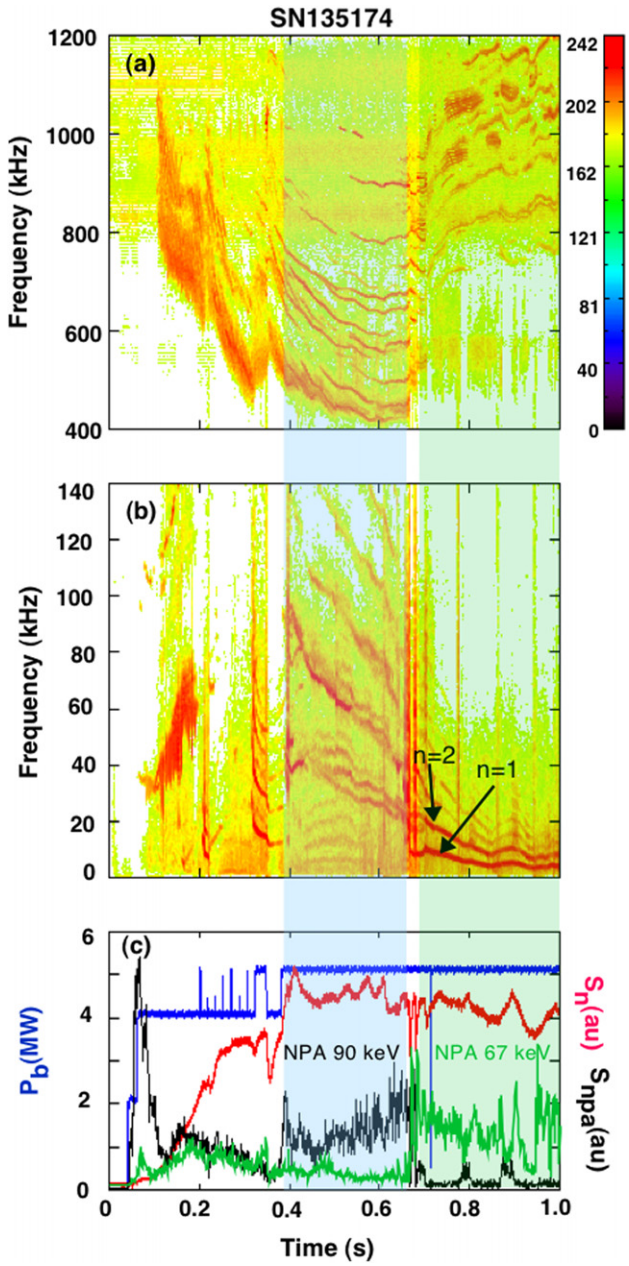

Figure 9. Mirnov spectrograms for SN135174 in the GAE/CAE (*a*) and the NTM/TAE (*b*) regimes plus waveforms showing the injected NB power, NPA signal at $E = 90$ keV and the volume neutron yield (*c*).

relatively constant at $Z_{\rm eff} \sim 1.3$ but subsequently ramps to at $Z_{\rm eff} \sim 2.0$ during the $E_{\rm b} = 67$ keV HEF. The effect of these profile changes on the neutron yield, $S_{\rm n}$ and total stored energy, $W_{\rm T}$, seen in figure 10(*e*) are obscured by sparse but strong ELM activity.

4. Alfvén eigenmode radial structure

As noted earlier, on NSTX the frequency evolution and amplitude of Alfvén modes are measured using a suite of diagnostics including Mirnov magnetic coils, BES [30], multichannel reflectometry [31], tangential collective high-k scattering [32], FIReTIP [33] and USXR [34] diagnostics. Unfortunately, two of the key diagnostics enabling MHD radial structure measurements, namely BES and 16-channel reflectometry, were unavailable until recently so it is necessary to utilize surrogate discharges that exhibit comparable MHD activity to those cited earlier.

Beam emission spectroscopy (BES) on NSTX provides ion gyroscale long-wavelength fluctuation measurements with $k_\perp \rho_{\rm i} < 1$ [30]. The measurements are spatially localized by intersection of the sightlines with the NSTX NBs. At this writing, ~10 channels spanning major radii from $R = 128$ cm to $R = 152$ cm near the equatorial mid-plane with spot size resolutions of 2–3 cm were available with an upgrade to 32 channels underway. In some discharges, preliminary spatial analysis has shown peaking of GAE modes near the plasma core with CAE and lower frequency modes further outboard. However, spatial mode structure results are not available for publication at this time pending completion of data and analysis validation procedures [41].

Figure 12 shows low-frequency ($f < 200$ kHz) MHD activity data for BES (*a*)–(*c*), Mirnov (*d*) and USXR (*e*)–(*g*) for SN138525. In the centre plot of panel (*h*), the 90 keV $S_{\rm npa}$

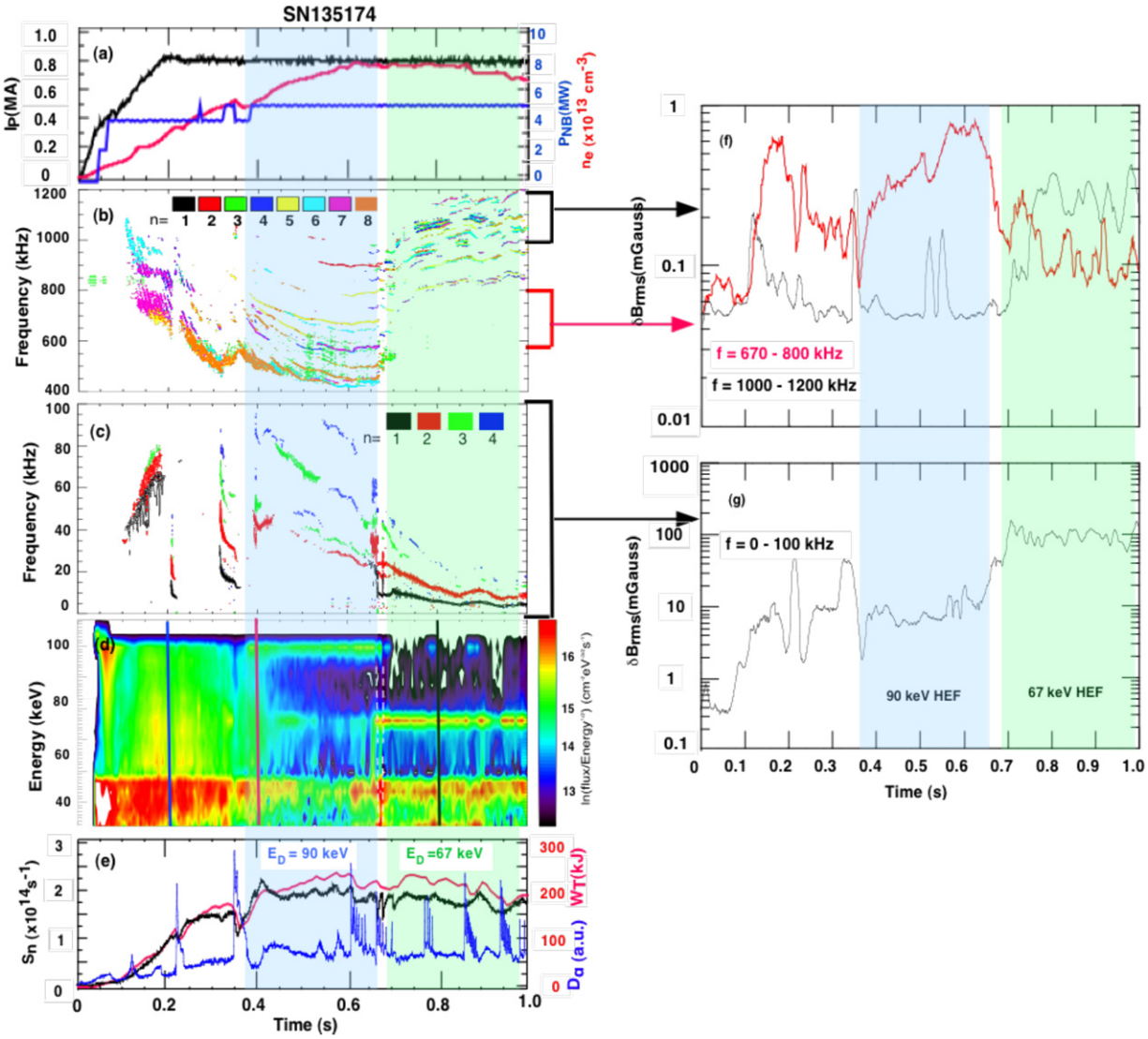

Figure 10. Selected plasma discharge data for SN1135174: (*a*) plasma current, injected NB power and MPTS line-average electron density, (*b*) MHD mode analysis for the GAE/CAE regime, (*c*) MHD mode analysis for the NTM/TAE regime, (*d*) contour plot of the NPA energetic-ion spectrum and (*e*) volume neutron yield, total stored energy and D_α emission. Mirnov spectra $\delta B_{\rm rms}$ amplitude plots are shown for selected high (*f*) and low (*g*) frequency bands.

signal (blue curve) is characteristic of a 'transient type' HEF comparable to SN132800 presented in section 3.1 that has a duration of ~100 ms and is attended by the usual excursion in neutron yield, $S_{\rm n}$ (black curve). Two massive edge localized mode (ELM) events on the D_α signal induce the sizeable transients seen on the $S_{\rm npa}$ and $S_{\rm n}$ waveforms. A shaded band in panel (*h*) demarks the HEF and its onset is translated to the other plots by a dashed line. In the BES, Mirnov and USXR traces it can be seen, as before, that the HEF occurs during a period that is devoid of low-frequency ($f < 20$ kHz) tearing or kink-type MHD activity. During the HEF interval, both the BES and USXR raw signals show that the TAE activity is localized towards the plasma outboard region as expected for these Alfvén eigenmodes [10, 42]. Although not shown, the Mirnov data exhibited substantial GAE activity in the range $f > 500$ kHz as in figure 5 for SN132800. Although BES has a Nyquist limit of 1 MHz [30], no evidence of such higher frequency modes was observed for this discharge.

The high-k collective microwave scattering system on NSTX [32] measures plasma density fluctuations at electron scale wave numbers ($k_\perp \rho_{\rm e} < 0.6$ and $k_\perp < 20\,{\rm cm}^{-1}$) and is deployed near the equatorial mid-plane with five detection channels having a radial resolution of $\Delta R \sim \pm 2$ cm and a frequency limit of $f \sim 3.25$ MHz. Steerable optics allow positioning of the scattering volume over a major radius range of $R \sim 110$–140 cm. In 2010, the high-k microwave power source was changed from ~300 mW carcinotron sources to ~30 mW solid-state sources thus reducing the scattered power by an order of magnitude compared with prior citations of high-k power scattering spectra [e.g. 43].

Figure 13 shows data for SN139395 that exhibited a transient HEF virtually identical to SN132800 discussed in section 3.1. The HEF interval, $t \sim 0.46$–0.57 s, is demarked by the shaded band and the red curve in figure 13(*a*) shows the NPA signal at $E = 90$ keV. Figure 14 shows high-k data for this discharge obtained with the

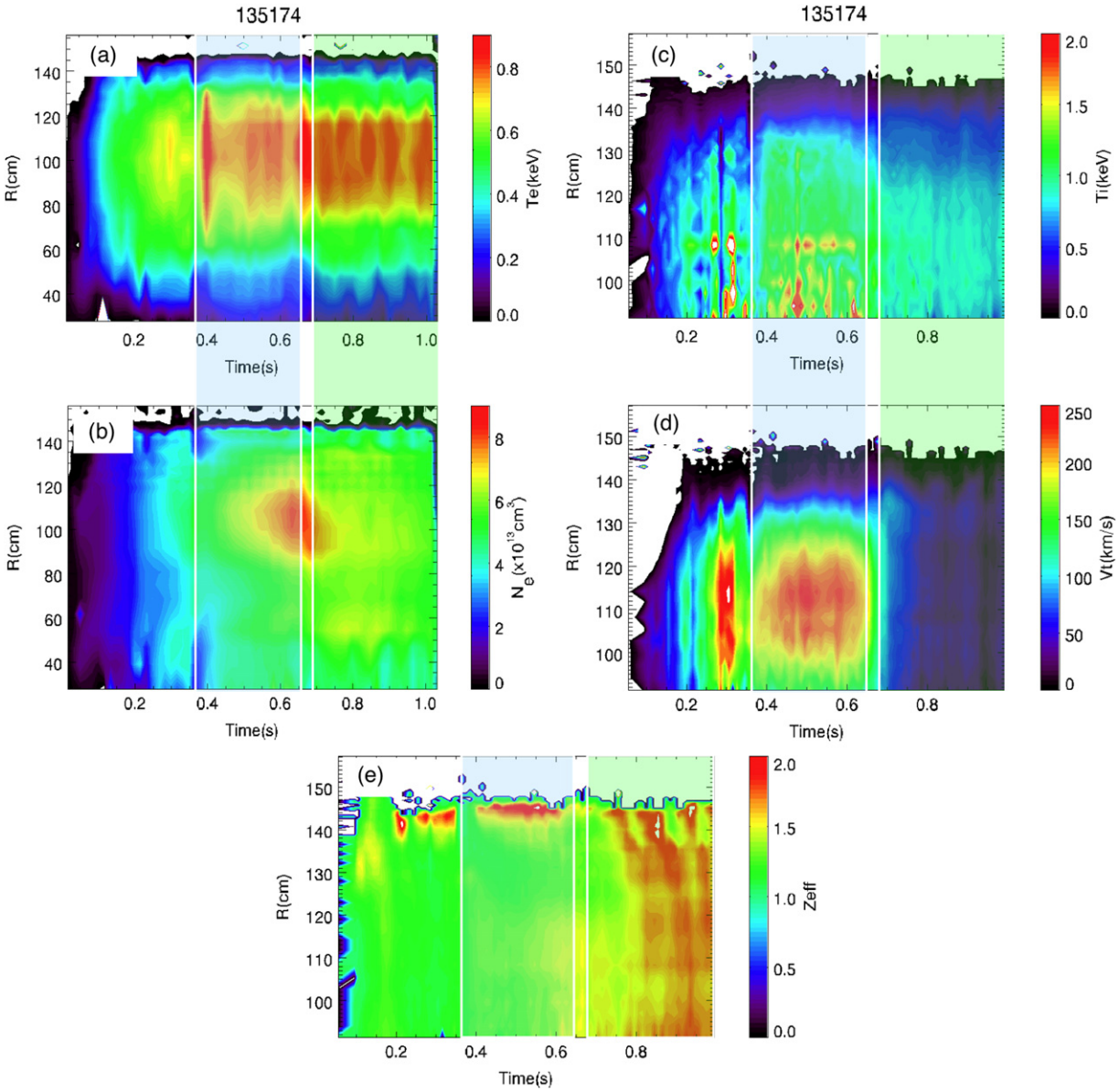

Figure 11. MPTS and CHERS contour plots for SN135174: (*a*) electron temperature, (*b*) deuterium ion temperature, (*c*) electron density, (*d*) toroidal rotation velocity and (*e*) carbon $Z_{\rm eff}$.

diagnostic line of sight tangent near the plasma core at $R = 116$ cm. Panel (*a*) shows GAE/CAE modes with $f \sim 1000$ kHz starting at $t \sim 0.34$ s with the overlaid red curve illustrating the time evolution of the scattered power integrated over modes in the range f(kHz) $\sim 1000 \pm 100$ kHz. In panel (*b*), the power spectra in interferometric mode at times demarked by vertical coloured lines in panel (*a*) show a growth in density fluctuations around $t \sim 0.44$ s. Assuming an integration path through the mode corresponding to the predicted toroidal extent [44], the fluctuation amplitude of the perturbed electron density is estimated as $\langle \delta n \rangle / \langle n \rangle \sim 2 \times 10^{-4}$, where the brackets indicate line-averaged values. A systematic radial scan of the high-k aiming relevant to the HEF study is not available and, given the GAE/CAE mode localization, the peak density perturbation amplitude might well be significantly higher. Unfortunately, corroborating BES data are not available because the mode frequency is up against the 1 MHz Nyquist limit of this diagnostic.

The NSTX reflectometer was recently upgraded to a 16-channel array that provides improved spatial sampling and access to the core of H-mode plasmas for monotonic density profiles [31]. The upgraded reflectometer consists of two eight-channel systems. Each system utilizes a single microwave circuit to generate a range of launch frequencies. One system operates with frequencies of 30, 32.5, 35, 37.5, 42.5, 45, 47.5 and 50 GHz while the other system operates with frequencies of 55, 57.5, 60, 62.5, 67.5, 70, 72.5 and 75 GHz. Both systems were configured to launch microwaves with O-mode polarization, so the microwaves launched into the plasma reflect where the plasma frequency is equal to the microwave frequency (i.e. at the O-mode cutoff). Consequently, the array of reflectometers reflects at densities in the range $n_{\rm e} = (1.1\text{–}6.9) \times 10^{13}$ cm^{-3}. Density perturbations associated with

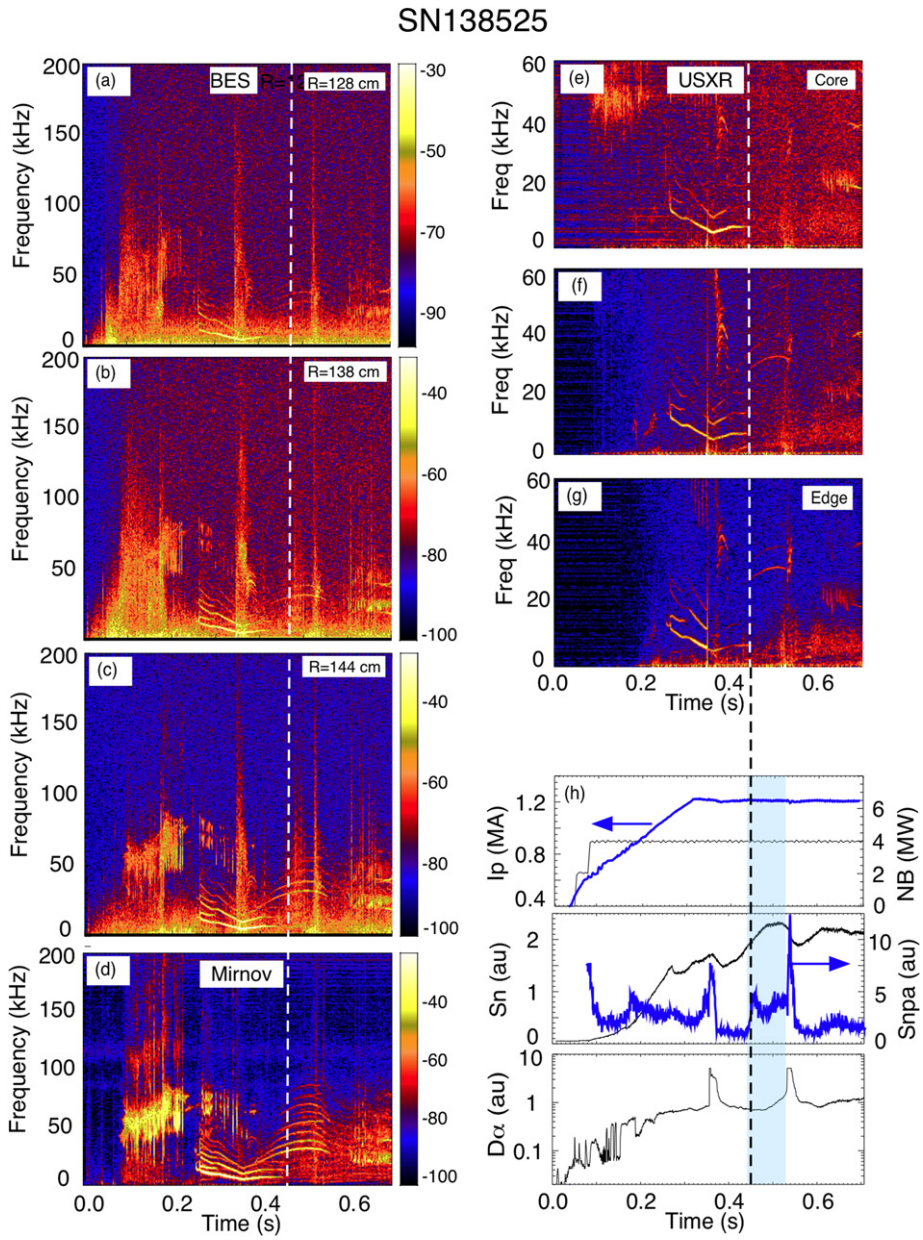

Figure 12. Beam emission spectroscopy (BES), Mirnov and USXR spectrograms for SN138525.

MHD modes in the plasma cause the optical path length of the microwaves to fluctuate. The effective radial displacement, ξ, defined as half the path length fluctuation is a good approximation of the cutoff surface displacement for global coherent density perturbations with large radial extent. The component of ξ that is coherent with the Mirnov coil edge magnetic fluctuations in the same frequency band is attributed to the mode. The incoherent component is used to estimate the statistical uncertainty. Since each frequency reflects at a different location, the array of path length fluctuations gives a measurement of the mode structure.

Since the upgraded reflectometry diagnostic was not available during the time frame of the discharges discussed in sections 3.1 and 3.2, it is necessary to utilize a surrogate discharge. For this purpose, reflectometry is applied to SN142508 shown in figure 15. Mirnov coil spectrograms for the high- and low-frequency ranges are displayed in panels (*a*) and (*b*), respectively. The NPA 90 keV signal exhibits an 'extended' HEF in the interval $t = 0.42$–0.72 s demarked by the shaded vertical band. In panel (*a*), the frequency range $f \sim 400$–800 kHz exhibits modes diverging or crossing in time that is a definitive signature of GAEs. The mode amplitudes of the high-frequency magnetic fluctuations, $\delta B_{\rm rms}$, are comparable to those cited earlier in figures 6 and 10. As seen in panel (*b*), HEF onset occurs after relaxation of $n = 1, 2$ NTM modes in accordance with earlier observations. The amplitudes of the low-frequency magnetic fluctuations, $\delta B_{\rm rms}$, during the HEF are somewhat larger (∼30%) relative to the earlier cases. Although not shown, the HEF strength, $H = F_{\rm max}/F_{\rm min} \sim 5$, is approximately one-half that for previous cases which could possibly be linked with larger amplitude of the TAE modes.

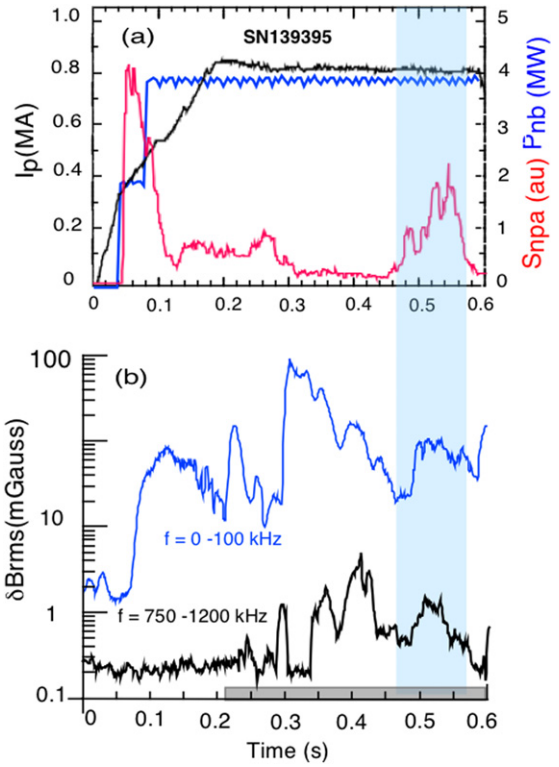

Figure 13. Waveforms for SN139395: (*a*) plasma current, NB power and NPA signal at $E = 90$ keV, (*b*) Mirnov coil fluctuation amplitude for selected frequency bands. The HEF is marked by a blue band and the high-k time window by a grey band.

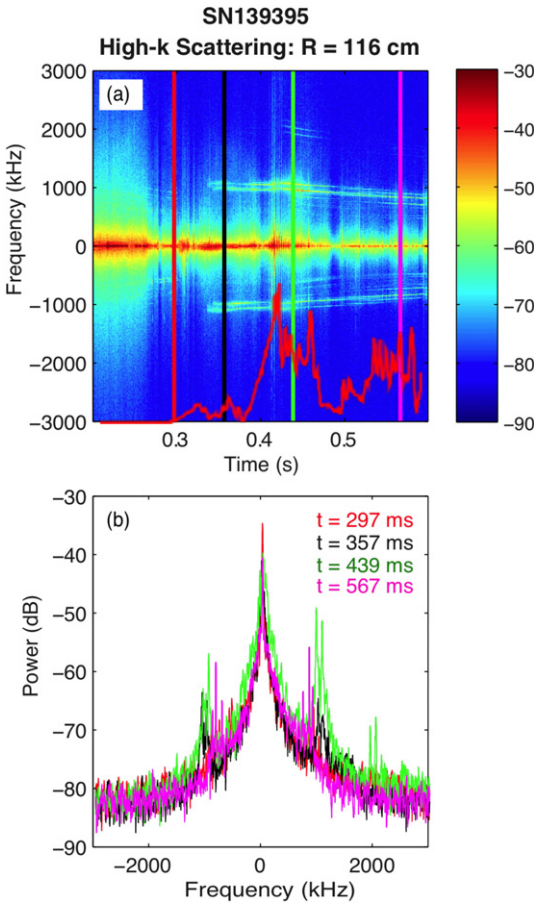

Figure 14. High-k scattering data for SN139395 showing robust GAE activity at $f \sim 1000 \pm 200$ kHz in the plasma core region, $R = 116$ cm: (*a*) frequency spectrogram with integrated power (au) shown by the red overlay and (*b*) power spectra in interferometric mode at selected times.

Figure 16 gives the reflectometer analysis for SN142508 at times before and during the HEF as marked by dashed lines in figure 15. For $t \sim 365$ ms prior to HEF onset, the amplitude of the effective radial displacement, $|\xi|$, is plotted against the cutoff radius with the modes separated into low- and high-frequency ranges in panels (*a*) and (*b*), respectively. Effective displacement approximates density contour displacement. In panel (*a*), the mode at $f = 14$ kHz is particularly robust (with a weaker harmonic at $f = 28$ kHz). The radial structure with large $|\xi|$ persisting to the plasma periphery can be interpreted as a core tearing mode coupled to an external kink mode [31]. In panel (*b*), the stronger modes in the frequency band around $f \sim 1000$ kHz are likely CAE modes. No modes were in the typical TAE range, $f \sim 50$–150 kHz. Corresponding data for $t \sim 548$ ms during the HEF are given in panels (*c*) and (*d*) that show only the strongest modes evident in figure 15, ignoring multiple weaker modes. In panel (*c*), the $f = 13$ kHz mode appears to be a residue of the kink mode noted above while the modes at $f = 50$ kHz and $f = 83$ kHz are relatively weak TAE modes. In panel (*d*), all the radial structures are consistent with robust core-localized GAE modes in the frequency range $f \sim 440$–800 kHz. As will be examined further in section 7, these modes appear to be driving the wave–particle interaction mechanism responsible for the formation of the HEF. The radial location of the reflectometer O-mode cutoffs mapped onto the MPTS density profile is shown in panel (*e*) for $t \sim 365$ ms and panel (*f*) for $t \sim 548$ ms. In these plots, the recorded MPTS density is scaled by a factor of 1.29 in order to align the observed reflection onset times for all channels of the reflectometer diagnostic. It is plausible that such scaling is required to compensate for a plasma-induced coating on the MPTS observation window or for proximate auxiliary gas puffing.

The FIReTIP diagnostic on NSTX for SN142508 had three tangential mid-plane chords operational with aiming tangency radii of $R_t = 85$, 132 and 150 cm [33]. As seen in figure 17, the chord at $R_t = 85$ cm exhibited GAE activity in the frequency range $f \sim 0.45$–0.95 MHz (with $\langle \delta n \rangle / \langle n \rangle \sim 10^{-4}$–$10^{-3}$) that is consistent with the Mirnov spectrogram in figure 15(*a*). Note that FIReTIP is a line integral measurement so these data alone do not localize the mode activity other than it exists somewhere between $R = 85$ cm and the plasma periphery. However, for the chord at $R_t = 132$ cm, this GAE activity is absent. and two CAE-like modes appear at $f \sim 0.95$ and $f \sim 1.05$ MHz, again consistent with figure 15(*a*). This indicates that the GAE modes exist inboard of $R = 132$ cm which agrees reasonably with the reflectometer data in figure 16(*d*). The most outboard chord at $R_t = 150$ cm exhibited no high-frequency activity.

The preceding mode radial structure data collectively leads to the following picture. Early robust kink/tearing modes near the plasma periphery at $f < 50$ kHz terminate at the HEF onset coincident with a transition to relatively weak outboard TAE activity at $f \sim 50$–150 kHz simultaneously with growth

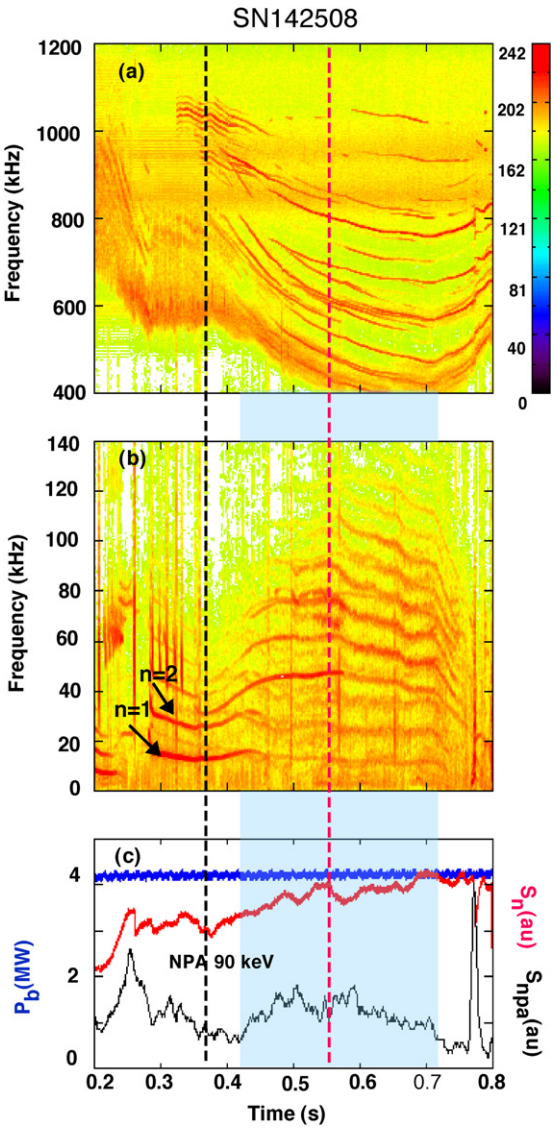

Figure 15. Mirnov spectrograms for SN142508 in the GAE/CAE (*a*) and the NTM/TAE (*b*) regimes plus waveforms showing the injected NB power, NPA signal at $E = 90$ keV and the volume neutron yield (*c*).

of robust core-localized GAE activity in the range $f \sim 400$–1000 kHz that persists for the duration of the HEF.

5. Overview of parametric dependences of the HEF

An overview of the NSTX operational scenarios, plasma discharge parameters and diagnostic observations related to the HEF is presented below, including effects such as lithium deposition on the NSTX plasma-facing components that are not documented in this paper due to space constraints. The HEF has not been clearly observed on NSTX confined energetic-ion diagnostics other than the $E\|B$ NPA, such as the vertical fast-ion D-alpha (vFIDA) [45, 46] and the solid state neutral particle analyser (ssNPA) [47] which is entirely understandable from their restrictions in terms of the acceptance range of $v_\|/v$ and/or insufficient energy resolution. For completeness, some aspects of HEF behaviour noted earlier are included in this overview.

5.1. $E\|B$ NPA observations

The HEF is observed as a transient increases in the NPA charge exchange flux localized at the NB full injection energy (never at the fractional energies) that exhibit peak-to-base flux ratios up to $H = F_{max}/F_{min} \sim 10 \pm 5$, rise-times of ~20–80 ms, durations up to hundreds of milliseconds and can turn on and off multiple times during a single discharge. HEFs have been observed for mid-plane NPA sightlines with: $R_{tan} \sim 55$–90 cm corresponding to a core-localized pitch range of $v_\|/v \sim 0.7$–0.9 measured by the NPA: i.e. passing energetic ions. The magnitude of the HEF flux approaches (but does not exceed) that of the NBI spectrum early in the discharge. Generally, ions are not accelerated above the NB injection energy and in rare exceptions the energy change is then $\Delta E/E < 4\%$ which challenges the $E\|B$ NPA instrumental energy resolution. Evolution of a slowing-down distribution below the HEF is rarely observed and then the evolution is very slow (hundreds of ms) compared with normal beam slowing-down times (tens of ms). HEFs do not produce a 'tail' such as observed in HHFW heating of beam-heated plasmas [47].

HEF ions transit the core region intersecting the NB footprint. This was verified using a programmed NBI power notch that caused prompt reduction of the HEF signal (i.e. on the timescale of beam primary neutral drop). However, due to large orbits, the HEF ions also traverse the plasma periphery as evidenced by ELM-induced modulations, corresponding to $v_\|/v \sim 0.5$–0.6 measured by the NPA, i.e. trapped energetic ions.

The NPA detector is a multi-anode microchannel plate array having 39 energy channels for both H and D species. By adjusting the analyser $E\|B$ fields, the HEF shifted to different detector anodes confirming that the HEF is not a NPA instrumental effect.

5.2. Global discharge conditions

The HEF is observed only in H-mode discharges (never L-modes) but not under all H-mode conditions. At a minimum, it is also required that $P_b \geqslant 4$ MW, $I_p \geqslant 0.8$ MA and weak MHD activity at $f < 100$ kHz. These appear to be necessary but not sufficient conditions for HEF occurrence. Short, unstable H-mode discharges with $P_b < 4$ MW plagued by early locked-mode events have been generated by manipulation of the NB power evolution and other discharge conditions. However, HEFs have never been observed under such conditions. HEFs have been observed mostly for $B_T = 4.5$ kG (with a few occurrences for $B_T = 5.0$, 5.5 kG) and $I_p = 0.8$–1.2 MA (not with lower I_p, B_T operation). HEF onset most frequently occurs in mid-discharge: e.g. $t > 0.4$ s and $n_e \geqslant 5 \times 10^{13}$ cm^{-3}.

5.3. MHD behaviour

The HEF is not observed in the presence of $f < 50$ kHz tearing or kink-type modes except for the lower energy $E \leqslant 70$ keV cases. HEF occurrence also requires that TAE activity ($f \sim 50$–150 kHz) is weak and global Alfvén eigenmode (GAE) activity ($f \sim 400$–1000 kHz) is robust. Compressional Alfvén eigenmode (CAE) activity ($f > 1000$ kHz) is usually

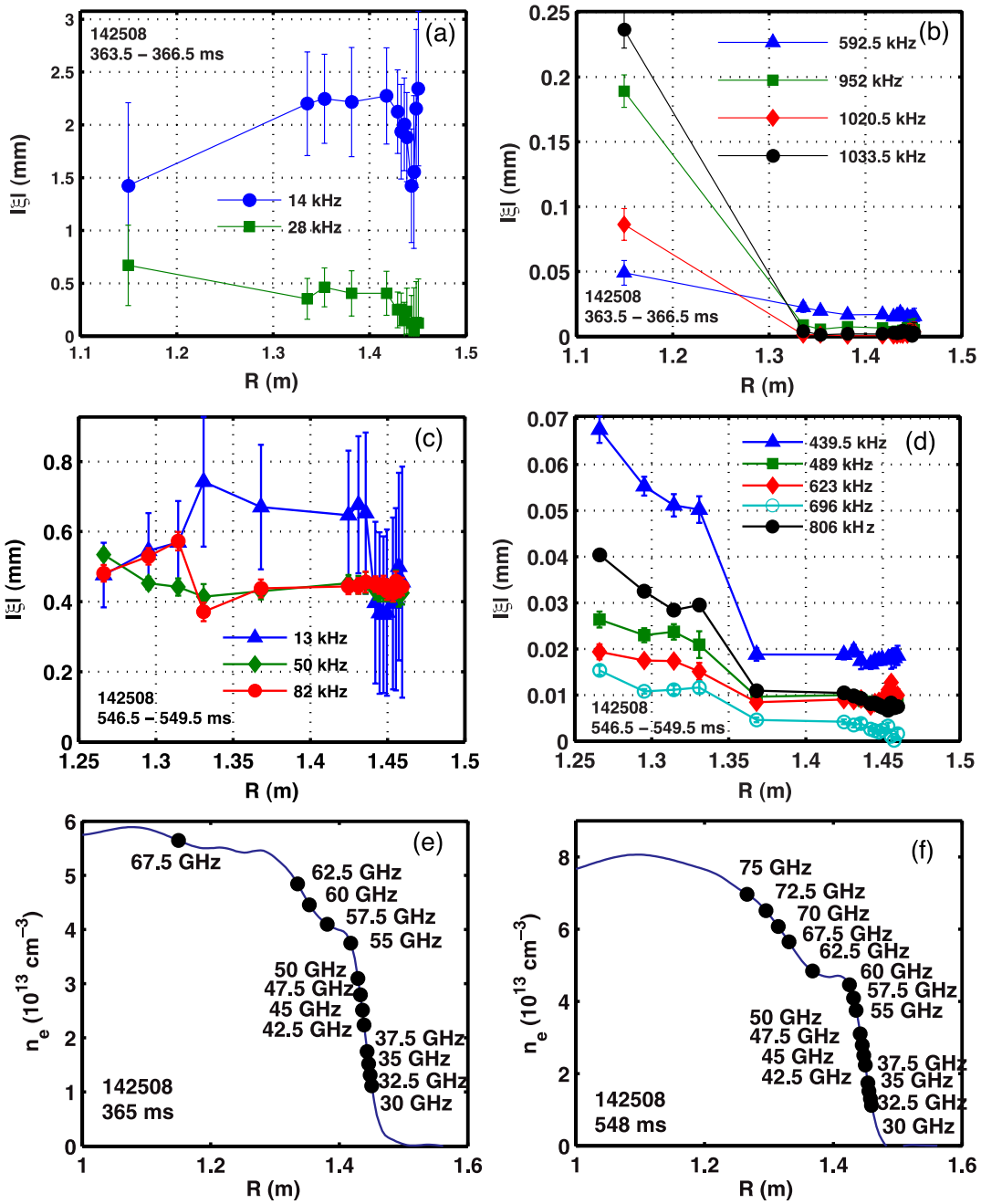

Figure 16. Multichannel reflectometry mode structure measurement for SN142508. Panels (*a*)/(*b*) are low/high frequency modes at $t = 365$ ms prior to onset of the HEF. Panels (*c*)/(*d*) are low/high frequency modes at $t = 548$ ms during the HEF. Panels (*e*)/(*f*) show the radial location of the mode measurements on the electron density profile.

sporadic or absent during the HEF event. MHD bursting events (e.g. EPM/TAE as well as internal reconnection events and/or sawteeth) modulate a wide range of energies including that of the HEF and usually terminate the HEF event. The amplitudes of the Mirnov signals in the GAE and CAE frequency range, $f \sim 400$–1500 kHz, do not show any bursting or other frequency modulation correlating with the HEF.

5.4. ELM effects

HEFs can occur with or without ELM activity. When present, ELMs can modulate the HEF amplitude by up to ∼30%: e.g. SN132800 comparing figure 6(*e*) showing ∼200 Hz ELMs with bursting on the $S_{\rm npa}$ signal in figure 5(*c*). The increase in HEF flux lags the ELM by ∼3 ms. This suggests that the ELMs release neutrals from the wall which then interact with HEF on the leg of the energetic-ion orbits that traverse the plasma periphery causing increased charge exchange flux. Thus the energetic-ion orbits associated with the HEF are inferred to traverse both the core and outer peripheral plasma regions, especially the outermost confined orbits as seen later in figure 26(*b*). The ELMS drive weak or no modulation of the NPA flux at energies below that of the HEF, presumably because such ions do not traverse the plasma periphery.

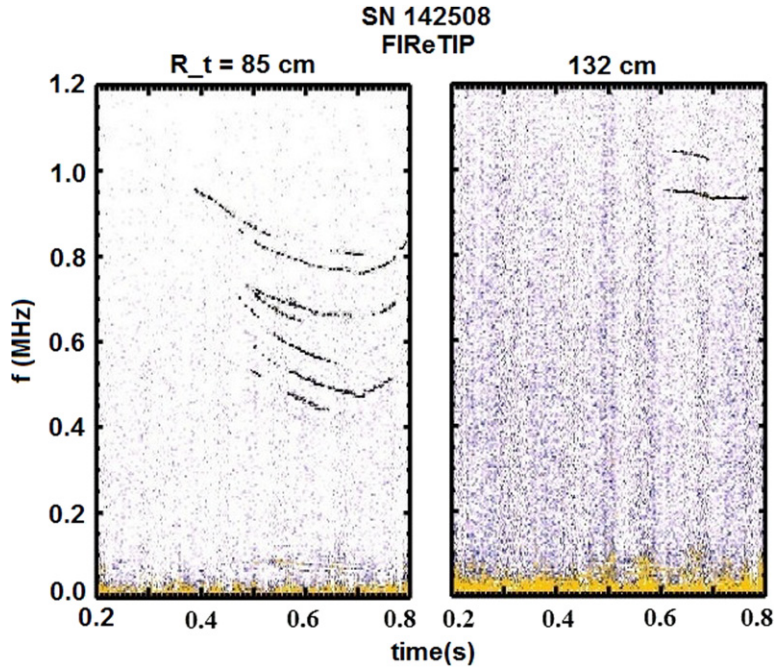

Figure 17. FIReTIP mode structure measurements for SN142508 at sightline aiming tangency radii, R_t, of 85 and 132 cm.

5.5. Lithium deposition effects

No HEFs are observed when lithium deposition on NSTX plasma-facing surfaces using the lithium evaporator (LiTER) [48] exceeds ~150 mg/shot or levels typically sufficient to modify the plasma performance including suppression of ELM activity [49]. HEFs progressively disappear as lithium deposition is increased to the noted level and can reappear as lithium effects wear off. The same behaviour is observed when lithium is applied using the lithium 'dropper' technique [50]. Why lithium deposition affects the HEF behaviour remains a subject of ongoing work, but the following conjectures can be offered. Firstly, the deposited lithium pumps the gas blanket surrounding the plasma. This reduces the edge neutral density and hence charge exchange production on HEF ions having orbits that traverse the plasma outer boundary region: i.e. suppresses the HEF flux. Secondly, lithium deposition leads to a strong elevation of $Z_{\rm eff}$ (e.g. from ~1 to ~6 during the discharge flattop of H-modes) due to a secular increase of carbon and medium-Z metallic impurities throughout the plasma volume. The elevated $Z_{\rm eff}$ will alter the energetic-ion pitch-angle scattering thus modifying the energetic-ion distribution in physical and phase space and hence possibly the HEF formation mechanism.

6. TRANSP code analysis

The TRANSP analysis code [51, 52] uses measured temperature and density (including impurity) profiles, rotation velocity and radiated power to compute the beam ion deposition and density using a Monte Carlo approach to determine the sources and losses of energy and particles. The NB ions can either be treated classically or MHD-induced loss and/or redistribution can be simulated using anomalous fast-ion diffusion (AFID). AFID has been applied, for example, to MHD-induced energetic-ion redistribution and/or loss effects in simulations of the $E \| B$ NPA spectra [13] including horizontal and vertical scanning measurements, in transport [53] and in beam-driven plasma current [3, 54]. In the following analysis, the TRANSP option to follow the fast-ion gyro-orbit is used (as opposed to the guiding centre).

The TRANSP code analysis for SN135174 applying the AFID model to the initial 90 keV source injection phase is presented in figure 18. The analysis is restricted to $t < 0.38$ s to focus on the early HEF with sources A and B at 90 keV and to avoid a distracting spectral component at $E \sim 67$ keV arising from the subsequent full turn on of source C. As shown in figure 18(*a*), the HEF does not appear on the simulated NPA spectrum calculated without imposition of AFID. This is consistent with the conjecture that the HEF is a wave–particle interaction phenomenon since TRANSP dos not model MHD activity. Application of AFID $= 20\,{\rm m}^2\,{\rm s}^{-1}$ leads to features that emulate the HEF as seen in panel (*b*). The AFID model had a flat profile over the minor radius with the energy dependence being full value for $50 \leqslant E\,({\rm keV}) \leqslant 84$ and zero for $E \geqslant 85$ keV. The AFID profile was ramped up to full value in the interval $t = 0.2$–0.3 s to provide equilibrated spectra around the selected time of interest, $t \sim 0.36$ s. Figure 18(*c*) shows the simulated NPA 2D spectra at $t = 0.36$ s for the range of AFID values: 0, 5, 10, 15 and $20\,{\rm m}^2\,{\rm s}^{-1}$. Figure 18(*d*) shows the calculated neutron yield for the associated AFID values along with the measured neutron yield for comparison.

While it can be argued that the AFID model qualitatively emulates the HEF, it clearly falls short in some key aspects. For the AFID $= 20\,{\rm m}^2\,{\rm s}^{-1}$ simulation, the 'peak-to-base' height factor, $H = F_{\rm max}/F_{\rm min} \sim 7$, is comparable to the measured value. However, the simulation does not exhibit the abrupt 'spike-on-tail' observed on the measured energy distribution as seen in figure 8(*b*) for $t = 400$ ms. On the other hand, in the simulation the peak of the HEF is constant and the growth

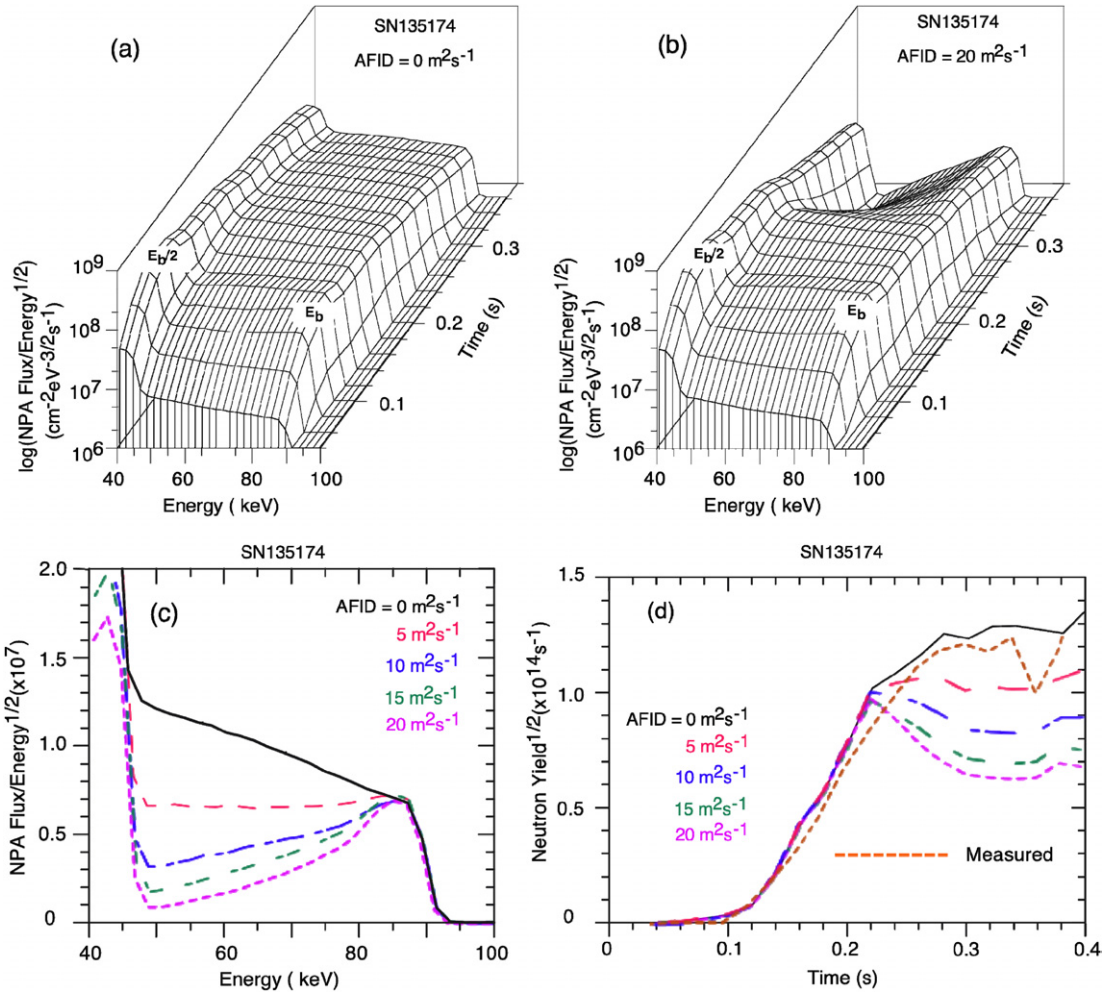

Figure 18. TRANSP code analysis for SN135174 employing AFID. With AFID $= 0\,\mathrm{m^2\,s^{-1}}$, the TRANSP-simulated NPA 3D energetic charge exchange spectrum (*a*) is clearly devoid of the HEF observed on the measured spectrum shown in figure 8. With AFID $= 20\,\mathrm{m^2\,s^{-1}}$ in panel (*b*), the 3D spectrum exhibits an energy dependence similar the HEF at $t > 0.2$ s. Panel (*c*) shows 2D simulated spectra for a range of AFID values as noted by the insert with the impact on the corresponding neutron yields shown in panel (*d*). AFID was flat over the minor radius and localized in energy to $50 \leqslant E(\mathrm{keV}) \leqslant 84$.

of the HEF 'height' factor is driven by depletion of the base slowing-down distribution consistent with measurements for SN135174. Numerous variations in the spatial and energy dependence of the AFID model failed to materially improve on the presented simulation. The most egregious shortcoming of the AFID model for attempted simulation of the HEF is the negative impact on conventional TRANSP results such as transport and power balance. This is clearly evident in figure 18(*d*) where the measured and calculated neutron yields agree reasonably without AFID, but depression of the neutron yield with AFID is unacceptable for all values utilized. Although not shown, the fast-ion power loss to the wall increased from 0.3 MW without AFID to 2.0 MW (half the injected beam power) with AFID $= 20\,\mathrm{m^2\,s^{-1}}$, consistent with the decrease in neutron yield but likewise unrealistic. Thus it must be concluded that the AFID model in TRANSP does not provide a satisfactory mechanism for simulation of the HEF phenomenon.

However, TRANSP analysis can be applied to shed light on another observation associated with the HEF: namely, excursions occurring in the neutron yield, S_n, and total storied energy, W_T, that appear to correlate with the HEF interval demarked by a blue band for SN132800 as shown in figure 19. It can be seen that the TRANSP calculations (dashed curves) closely reproduce the time evolution and magnitude of the measured excursions in S_n and W_T in this discharge. It will be demonstrated momentarily that the changes in S_n and W_T are driven by increases in the core T_e, n_e, T_i and n_D (all of which are measured inputs). Note that during the time of interest, T_e also develops a broad profile with steep inboard and outboard radial gradients as shown in figure 7(*a*).

Figure 20 serves to demonstrate that the behaviour of S_n and W_T noted in the preceding figure is not related to the HEF phenomenon. SN132181 is a HEF-free discharge (see panel (*d*)) with a strong increase in measured and calculated S_n and W_T as seen in panel (*e*) that occur in the interval marked by the vertical grey band. The absence of a HEF is attributed to the low plasma current, $I_\mathrm{p} = 0.7$ MA (it being noted in section 5.2 that the HEF has been observed only for $I_\mathrm{p} \geqslant 0.8$ MA). Panel (*c*) shows that this interval is devoid of $n = 1$ kink-type MHD and the TAE activity is minimal as is typical for discharges that do exhibit HEF

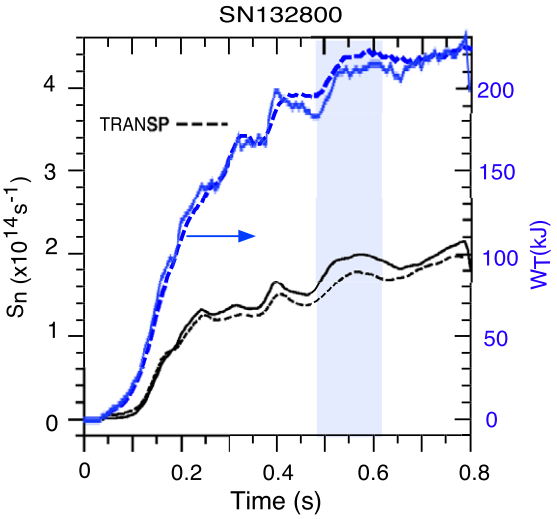

Figure 19. Comparison of measured and calculated neutron yield and total stored energy for SN132800.

events. A strong increase in electron temperature concurrent with the increases in S_n and W_T is evidenced in panel (b). Although not shown, concurrent significant increases also occur in the measured core T_e, n_e, T_i and v_ϕ. Other aspects of the TRANSP analysis such as transport and power balance are 'normal' but further details are outside the scope of this section. The causal interpretation is that reduced low-frequency MHD activity results in improved confinement that, in turn, is the driver for plasma profile changes producing the noted excursions in the measured and calculated S_n and W_T parameters. Hence it is concluded that the S_n and W_T excursions are driven by plasma profile changes induced by changes in MHD activity and not the HEF phenomenon itself. Nevertheless, such plasma profile changes could still bear some correlation with the HEF phenomenon since they may in part be responsible for driving fast-ion redistribution associated with the HEF in conjunction with a direct wave–particle interaction mechanism.

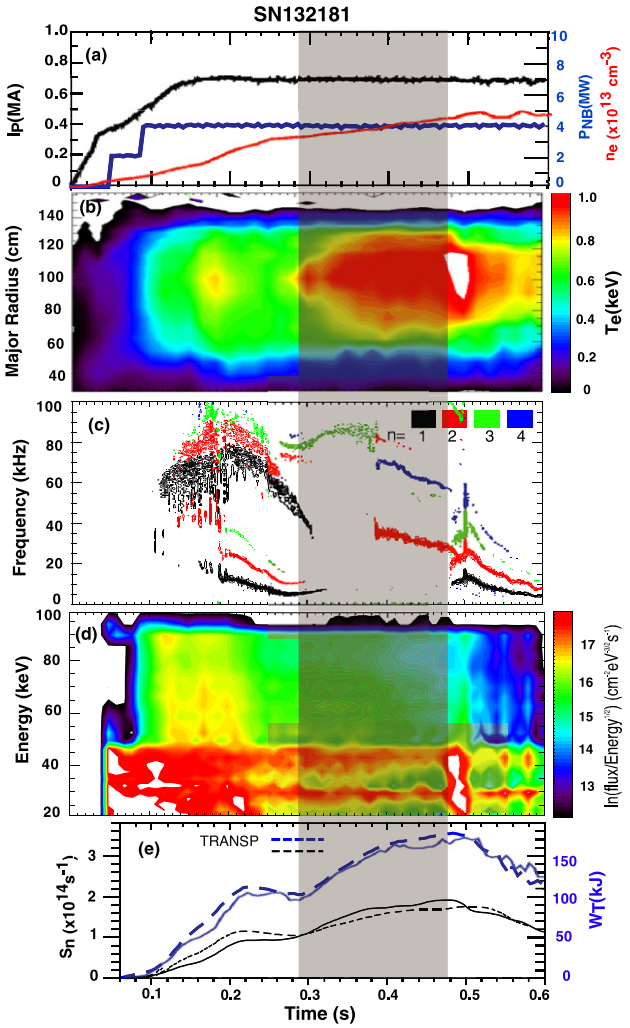

Figure 20. Selected plasma discharge data for SN132181: (a) plasma current, injected NB power and MPTS line-average n_e, (b) MPTS T_e contour plot, (c) MHD mode analysis for the NTM/TAE regime, (d) NPA energetic-ion flux contour plot and (e) comparison of measured (solid lines) and TRANSP-calculated (dashed lines) volume neutron yield and total stored energy.

7. Mechanisms of HEF formation

In this section, candidate mechanisms for HEF formation are developed based on quasilinear (QL) theory of wave–particle interaction.

7.1. Effects of Coulomb collisions on the distribution function of energetic ions

The maximum energy of the injected ions ($E_b = 90\,\mathrm{keV}$) well exceeds $T_e(M_i/M_e)^{1/3}$ (where T_e is the electron temperature, M_i and M_e are the ion mass and electron mass, respectively). In this case the main effect of Coulomb collisions on ions with $E \sim E_b$ is the drag produced by the electrons, whereas the effects of ion drag and pitch-angle scattering are small. Neglecting the pitch-angle scattering leads to $F_b(E) \propto E^{-3/2}$. However, strictly speaking, neglecting pitch-angle scattering is justified provided that the energetic-ion source is isotropic in velocity space. Otherwise, Coulomb pitch-angle scattering will lead to a depleted particle population at the pitch angles of injection, thus decreasing the slope of $F_b(E)$ at these pitch angles. This effect can be significant when the pitch-angle width ($\delta\chi$ with $\chi \equiv v_{||}/v$) of the injected ion distribution is sufficiently narrow because the effective time of the scattering is proportional to $(\delta\chi)^2$. The presence of impurities makes $F_b(E)$ flatter, thus enhancing the scattering. In the event that the scattering might be very strong, a HEF could arise. Specific calculations are required to clarify the role of pitch-angle scattering in the NSTX experiments. For this purpose we write the following equation [55]:

$$\frac{\partial F_b}{\partial t} = \frac{1}{\tau_s^e v^2}\frac{\partial}{\partial v}[(v^3 + v_c^3)F_b] + \frac{\alpha}{\tau_s^e}\frac{v_c^3}{v^3}\frac{\partial}{\partial \chi}(1-\chi^2)\frac{\partial F_b}{\partial \chi} + S(r, v, \chi) + \frac{1}{r}\frac{\partial}{\partial r} r D_r \frac{\partial F_b}{\partial r}, \quad (1)$$

where τ_s^e is the beam slowing-down time associated with electrons, $S(r, v, \chi)$ is the source term describing the injection, the last term describes the radial diffusion with r the radial

coordinate and D_r the diffusion coefficient,

$$v_c = \left(\frac{3\sqrt{\pi}}{4}\frac{M_e}{n_e}\sum_i \frac{n_i Z_i^2}{M_i}\right)^{1/3} v_{T_e},$$

$$\alpha = \frac{n_e Z_{ef}}{2M_b \sum_i n_i Z_i^2/M_i}, \qquad (2)$$

$v_{T_e} = \sqrt{2T_e/M_e}$ and Z_i, Z_{ef} are the ion charge number and the effective charge number, respectively. Note that the product αv_c^3 is actually the pitch-angle scattering rate. Then, solving equation (1) with

$$S \propto \sum_{j=1}^{2} \exp\left[-\frac{(\chi - \chi_{bj})^2}{(\delta\chi)^2}\right]\delta(E - E_b) \qquad (3)$$

and $D_r = 0$, where χ_{b1} and χ_{b2} characterize the particle sources due to two injection beams, we obtain the picture shown in figure 21(*a*). We observe that the energy dependence of the injected ion distribution at $\chi = \chi_{b1}$ is considerably weaker than $E^{-3/2}$. Numerical modelling with the TRANSP code confirms this, giving even a weaker dependence of F_b on E as shown in figure 21(*b*). However, the difference between figures 21(*a*) and (*b*) is weak which indicates that the role of the neoclassical radial transport neglected in equation (1) is not crucial.

A general conclusion following from the above is that Coulomb pitch-angle scattering in NSTX experiments was not sufficient to produce a non-monotonic energy dependence of the injected ion distribution. Therefore, below we consider effects of plasma instabilities.

7.2. Instabilities in discharges exhibiting the HEF

Alfvénic instabilities in NSTX discharges where HEFs were observed (and in many other discharges) can be divided into three groups, depending on their frequencies and temporal evolution: (i) low-frequency (LF) instabilities with frequencies in the range of $f \sim$ 20–100 kHz; (ii) high-frequency (HF) instabilities with $f \sim$ 500–1000 kHz; (iii) very high frequency (VHF) instabilities, $f \sim$ 1000–2000 kHz, as shown in figure 22. As seen from this figure, maxima of the perturbed magnetic field (δB) at the plasma edge during HF instabilities (accompanied by the HEF formation) correspond to minima of δB associated with LF instabilities. In addition, there is correlation between maxima of δB associated with LF and VHF instabilities, but this is not necessarily the case in other discharges. The described three groups of instabilities may have different effects on the energetic ions.

In order to understand the role of the observed instabilities, we need to identify them. Noticing that the frequencies of the HF and VHF perturbations well exceed those of the TAE (toroidicity-induced Alfvén eigenmodes) instabilities, we conclude that the HF and VHF instabilities are either destabilized GAE (global Alfvén eigenmodes) modes or CAE (compressional Alfvén eigenmodes) modes. On the other hand, the HF instabilities could hardly affect the distribution function of the energetic ions if their amplitudes were as small as those shown in figure 22. The high-k collective scattering measurements presented in section 4 seem to confirm that the amplitudes of the HF instabilities were much larger. This suggests that the HF perturbations were core-localized. We conclude from here that the HF instabilities were probably destabilized GAE modes because the CAE modes are normally located towards the plasma periphery.

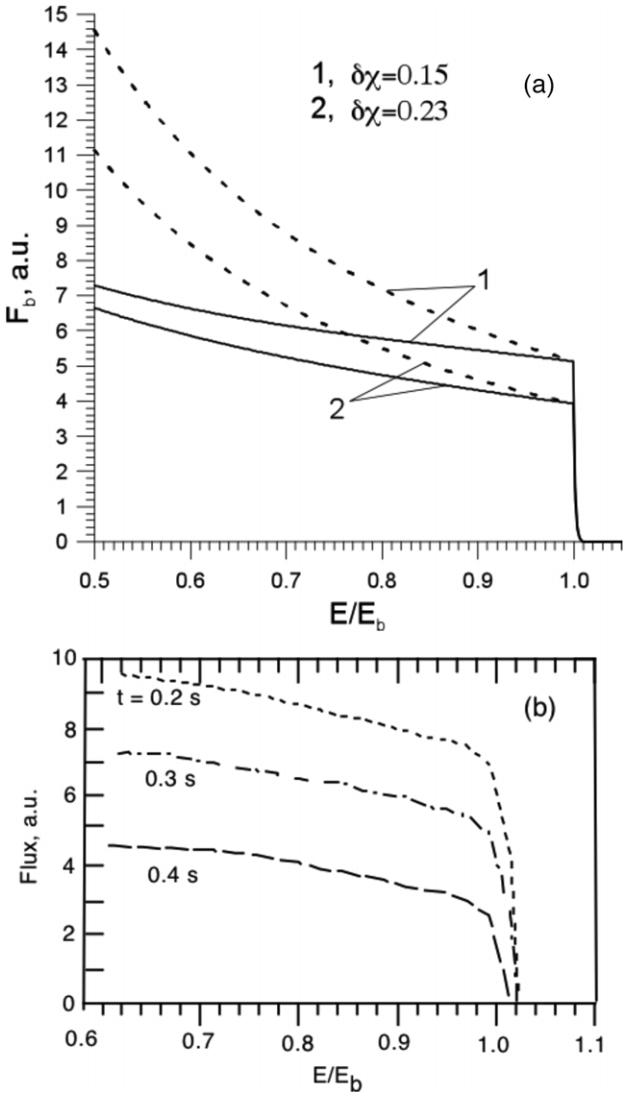

Figure 21. Distribution function of the energetic ions. Panel (*a*): solid lines show solutions of equation (1) for two different pitch-angle widths of the injection beams at $\chi = 0.73$ (which is close to the middle of one of the NSTX beams) in the absence of instabilities and radial diffusion; dashed lines show slowing-down distributions, $F_b(E) \propto E^{-3/2}$. Panel (*b*) shows the result of a TRANSP calculation.

7.3. Bounce-averaged equation of QL theory

We investigate the influence of Alfvénic instabilities on the distribution function of the energetic ions by means of a QL theory equation averaged over the particle bounce/transit time, τ_b, which can be written as follows [56]:

$$\frac{\partial F_b}{\partial t} = \frac{1}{\tau_b}\sum_{m,n,l} \hat{\Pi} D \hat{\Pi} F_b + C^{Col}, \qquad (4)$$

where $F_b = F_b(E, \mu, r, t)$, μ is the particle magnetic moment, P_φ is the canonical angular momentum,

$$\hat{\Pi} = \frac{\partial}{\partial E} + \frac{l\omega_B}{\omega B_0}\frac{\partial}{\partial \mu} - \frac{n}{\omega}\frac{\partial}{\partial P_\varphi}, \qquad (5)$$

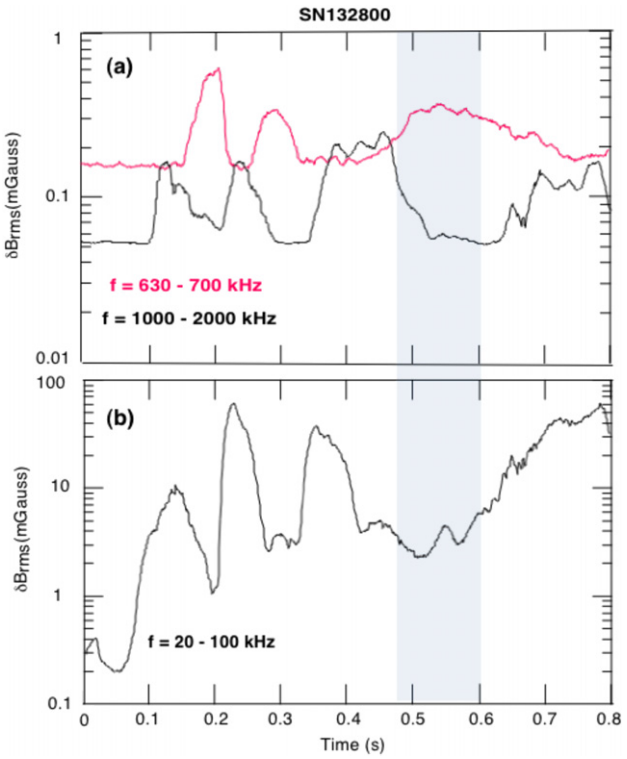

Figure 22. Amplitudes of instabilities detected on Mirnov coils in NSTX discharge SN132800. The HEF occurs during the period of 0.5–0.6 s (marked with a band).

where ω is the mode frequency, ω_B is the bounce-averaged particle gyrofrequency, the subscript '0' refers to the magnetic axis, m and n are the mode numbers, q is the safety factor, $D = \pi e^2 \sum_s |J_s|^2 \delta(\Omega)$,

$$\Omega = \omega - l\omega_B - (m+s)\omega_b + \omega_\varphi, \tag{6}$$

where $\omega_b = 2\pi/\tau_b$, s and l are integers, ω_φ is the frequency of the particle motion in the toroidal direction, $\delta(x)$ is the Dirac delta function, ϑ is the poloidal angle, φ is the toroidal angle, J_s is a quantity proportional to square of the wave amplitudes and depends on particle orbits in the equilibrium magnetic field (see [56]), C^{Col} is the collision term and e is the ion charge. The perturbations are taken in the form $\delta X = \hat{X}(r)\exp(-i\omega t - in\varphi + im\vartheta)$. It follows from equation (4) that the waves directly affect only particles satisfying the resonance condition $\Omega = 0$ and that the QL evolution of F_b is determined by the characteristics of the equation $\hat{\Pi} F_b = 0$.

The influence of QL-diffusion on the distribution function F_b is considerable only when the amplitudes of the destabilized waves are sufficiently large to compete with Coulomb slowing down of the energetic ions. In order to make estimates, we introduce the diffusion coefficients D_v, D_r, and D_χ which describe the QL evolution over velocity (v), radius (r) and pitch angle (χ). One can see that these coefficients are connected with D as follows:

$$D_v = \frac{D}{M^2 v^2}, \qquad D_\chi = D\left[\frac{1}{Mv^2\chi}\left(\frac{l\omega_B}{\omega} + \chi^2 - 1\right)\right]^2,$$
$$D_r = \left(\frac{k_\vartheta}{M\omega\omega_B}\right)^2 D \tag{7}$$

$k_\vartheta = (m+s)/r$. Then QL-effects can be significant provided that at least one of the conditions below is satisfied:

$$\tilde{D}_v \equiv \frac{D_v \tau_s^e}{v^2} > 1, \qquad \tilde{D}_\chi \equiv D_\chi \tau_s^e > 1,$$
$$\tilde{D}_r \equiv \frac{D_r \tau_s^e}{a^2} > 1. \tag{8}$$

We find from equations (7) and (8):

$$\frac{\tilde{D}_r}{\tilde{D}_v} = \left(\frac{k_\vartheta v}{\omega}\frac{\rho}{a}\right)^2, \qquad \frac{\tilde{D}_\chi}{\tilde{D}_v} = \frac{1}{\chi^2}\left(\frac{l\omega_B}{\omega} + \chi^2 - 1\right)^2. \tag{9}$$

It is clear that equations (9) are valid when the same type of resonance is responsible for D.

7.4. Analysis of resonances between the destabilized modes and injected ions in NSTX

The HEF was observed at $\chi = 0.7$–0.9 and the poloidal angle $\vartheta = \pi$ corresponding to the high-field side of the torus (more specifically, on the high-field side of the Shafranov-shifted magnetic axis where the NPA flux is spatially localized by the injected beam neutrals as noted in section 2). At this poloidal angle the pitch angle is a minimum on the particle orbit. Therefore, we consider the resonance for circulating particles only. In this case, the equation $\Omega = 0$ is reduced to

$$\omega = (1 + s\lambda^{-1})k_\parallel v_\parallel + n\omega_D + l\omega_B, \tag{10}$$

where ω_D is the frequency of the ion toroidal precession, $\lambda = k_\parallel q R_0$, q is the safety factor, R_0 is the major radius of the torus and $k_\parallel = (mq^{-1} - n)/R_0$ is the longitudinal wave number.

For well-circulating particles the precession frequency is relatively small; it will be neglected in the qualitative analysis below. On the other hand, the cyclotron resonance ($l \neq 0$) is not possible when $\omega \ll \omega_B$. Therefore, energetic particles interact with the LF waves only through the $l = 0$ resonance. The role of the $l \neq 0$ resonance in HF and VHF instabilities is not so clear because the ratio ω/ω_B is not very small (for instance, $\omega/\omega_B = 0.3$ when $f = 1$ MHz, $B = 0.45$ T and the ion is deuteron). In order to clarify this point, we take into account that the Alfvén velocity $v_A \sim 10^8$ cm s^{-1} in the core region of NSTX deuterium plasmas and the maximum velocity of the injected ions is $v_b = 3 \times 10^8$ cm s^{-1} which implies that the HEF in the high-energy region is formed by particles with $v \sim 3v_A$. Taking this into account, we consider only the resonant particles with $v_\parallel \geqslant v_A$. Then, in the case of Alfvén waves ($\omega = k_\parallel v_A$), the minimum mode frequency satisfying the resonance condition with $l \neq 0$ and $s \sim 1$ is associated with the $l = 1$ resonance and is given by [57]

$$\omega_{min} = \frac{\omega_B I_s}{|v_\parallel|/v_A + 1}, \tag{11}$$

where $I_s = 1 - |s|\rho_b/(qR_0)$, $\rho_b = v_b/\omega_B$ and $k_\parallel v_\parallel < 0$. Taking $I_s \approx 1$ and $v_A = 2.94 \times 10^8$ cm s^{-1}, we obtain

$$\omega_{min}(\chi = 0.7) = 950\,\text{kHz}, \qquad \omega_{min}(\chi = 1) = 730\,\text{kHz}. \tag{12}$$

Note that equation (12) gives frequencies in the plasma frame. The observed frequencies are lower due to Doppler shift ($f_{Doppler} \sim 30n$ kHz in the core in many NSTX discharges). It follows from our analysis that HF instabilities interact with the energetic ions through both $l = 0$ and $l = 1$ resonances.

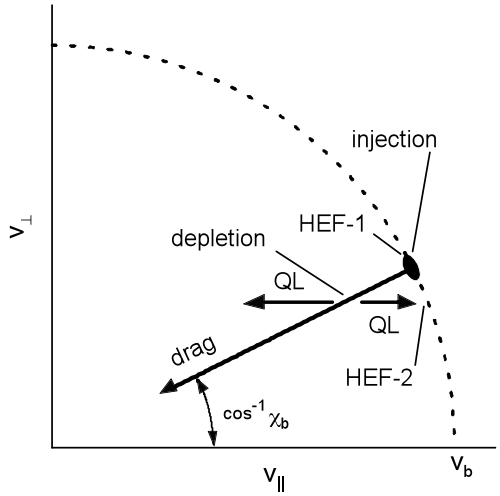

Figure 23. Sketch explaining the formation of a HEF in $F_b(v, \chi)$ when the magnetic moment is conserved and spatial diffusion is not important. Here arrows noted by 'QL' show the directions of QL diffusion. The places where a HEF arises are shown by labels 'HEF-1' and 'HEF-2'.

7.5. The HEF caused by QL distortion of F_b in velocity space

Below we consider the effects of the $l = 0$ and $l = 1$ resonances on the QL distortion of F_b in velocity space.

First let us consider effects of the $l = 0$ resonance. One can see that particles affected by the LF instabilities and particles affected by the HF instabilities through the $l = 0$ resonance are different. The matter is that $\lambda < 1$ for the LF instabilities, whereas $\lambda \gg 1$ for the HF instabilities. A simple estimate shows that the LF instabilities can be identified as TAE modes. Indeed, $\lambda = 1/2$ for the TAE modes from which it follows that $f^{\rm TAE} \leqslant 40$ kHz when $q \geqslant 2$ which was the case, for example, in discharge SN132800. If so, the LF instabilities affect energetic ions mainly through the $s = 1$ resonance that tends to distort the distribution function of the injected ions (F_b) in the vicinity of $v_\parallel = v_A$ and $v_\parallel = v_A/3$. In addition, relatively weak interaction between TAE modes and energetic ions with $v_\parallel \sim v_A$ is possible due to the finite mode width and the magnetic shear. Resonances with $s > 1$ involve particles with lower energies in the case of TAE modes. This simple analysis shows that TAEs cannot lead to a HEF when $v_b \gg v_A$. In contrast to this, the HF instabilities can affect $F_b(v)$ at $v \sim v_b$ due to the $s > 1$ resonances. For instance, for $s = 2$ and $v_\parallel/v_A = 2$ we obtain $\lambda = 4$ from the resonance condition which corresponds to $f = 640/q$ kHz in the case of $\omega = k_\parallel v_A$. This is within the frequency range of the HF instabilities because usually $q_0 > 1$ or $q_0 \sim 1$ during the HEF (for instance, $q_0 \sim 1.5$ during the HEF in discharge SN132800 with the region of $q \approx$ const being rather wide in the plasma core).

Equation (4) shows that the QL diffusion with $l = 0$ conserves the particle magnetic moment (i.e. roughly speaking, $v_\perp \approx$ const during the QL-diffusion). Thus, like Coulomb pitch-angle scattering, it competes with the collisional drag for which $\chi \approx$ const. This means that the QL-diffusion in velocity space tends to produce the HEF provided that resonances exist in the region $v \sim v_b$. Moreover, as seen from figure 23, QL diffusion may lead to two kinds of HEF. One of them, HEF-1, is characterized by a depleted velocity region with $v < v_b$ at the pitch angles of injection ($\chi_{\rm inj}$). HEF-2 arises at $\chi > \chi_{\rm inj}$ because the QL-diffusion delivers particles to this region. This means $F_b(v \approx v_b)$ exceeds that in the absence of the waves in the case of HEF-2.

In order to model numerically the effects of joint action of Coulomb collisions and QL-diffusion with $l = 0$ in the absence of the radial diffusion (i.e. when the first term in $\hat{\Pi}$ dominates), we have written equation (1) in the $(v, v_\perp)$-variables and taken the energy diffusion artificially large. We observed both HEF-1 and HEF-2 types, but the HEF 'height', $H \equiv F_{b,\max}/F_{b,\min}$, was small. Therefore, the considered mechanism cannot explain the formation of HEFs with large height, $H \sim 8 \pm 5$, that were observed in many NSTX discharges.

When instabilities are driven by the spatial gradient of energetic ions, the terms with radial derivative dominate in equation (4). One could expect that the analysis above is not applicable to this case. However, this is not necessarily true. The matter is that there is a region with $\nabla \cdot \mathbf{\Gamma} \approx 0$ ($\mathbf{\Gamma}$ is the flux of the resonant energetic ions across the magnetic field) between the regions where $\nabla \cdot \mathbf{\Gamma} > 0$ and $\nabla \cdot \mathbf{\Gamma} < 0$ due to finite width of the location of the instability. One can expect that the HEF in this region will be formed due to velocity diffusion. In addition, instabilities may lead to a local flattening of the radial profile of the energetic ions that increases the role of the velocity diffusion.

Now let us consider the effect of the $l = 1$ resonance. As seen from figure 23, the angle between the lines $\mu \approx$ const and $\chi \approx$ const is small when $\chi \sim 1$. In contrast to this, the angle between the lines $\chi \approx$ const and the characteristics of the QL operator with $l = 1$ is large. Due to this, we can model the QL-relaxation in velocity space when $l = 1$ by means of equation (1), assuming that $D_r = 0$, whereas α is large, being caused by the waves. We have found that the height of the HEF arising in this case can be considerable provided that the pitch-angle distribution of the injected ions is narrow. However, the height is less than that observed in experiments even for beams with an unrealistically narrow distribution over pitch angles and an unrealistically large resonance region as shown in figure 24.

7.6. The role of anomalous spatial diffusion in HEF formation

It is now clear that spatial diffusion must be taken into account to explain the formation of HEFs with large H. Note that the fact that transport of fast ions leading to the loss of these ions can result in a non-monotonic dependence of $F_b(E)$ is known due to 0D calculations [58]. The function $F_b(E)$ becomes strongly non-monotonic when $\tau_n \ll \tau_s$, where τ_n is the confinement time of the energetic ions, which is the same as $\tilde{D}_r \gg 1$. However, if $\tau_n \ll \tau_s$, almost all the injected energy is lost to the wall. Clearly, this was not the case in the experiment. When $\tilde{D}_r \sim 1$, the spatial diffusion leads to a small HEF. Moreover, when the beam distribution is strongly peaked and $\tilde{D}_r \sim 1$, the HEF arises only near the plasma centre, not in the periphery. Figure 25 obtained by solving equation (1) with anomalous D_r demonstrates this. This means that when $F_b(r)$ is strongly peaked, radial diffusion with $\tilde{D}_r \sim 1$ cannot result in the HEF observed by the NPA.

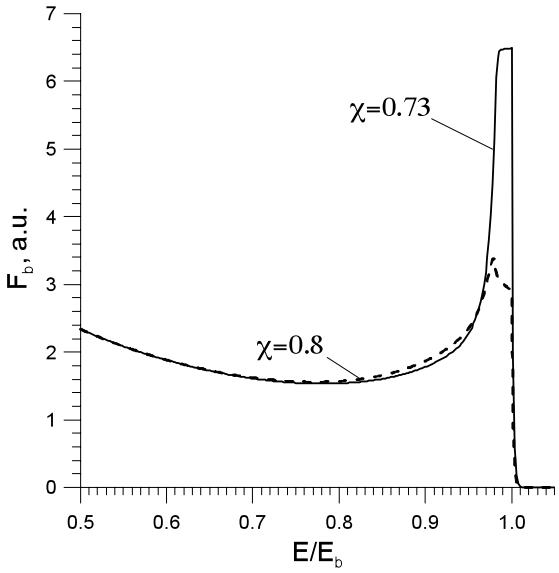

Figure 24. Effect of anomalous pitch-angle diffusion on $F_b(E)$. Here $\tilde{D}_\chi = 10(1-\chi^2)$ for $0.95 < v/v_b < 0.98$, the pitch-angle distribution of injected particles is given by equation (3) with $\chi_{b1} = 0.6$, $\chi_{b2} = 0.72$ and $\delta\chi = 0.1$.

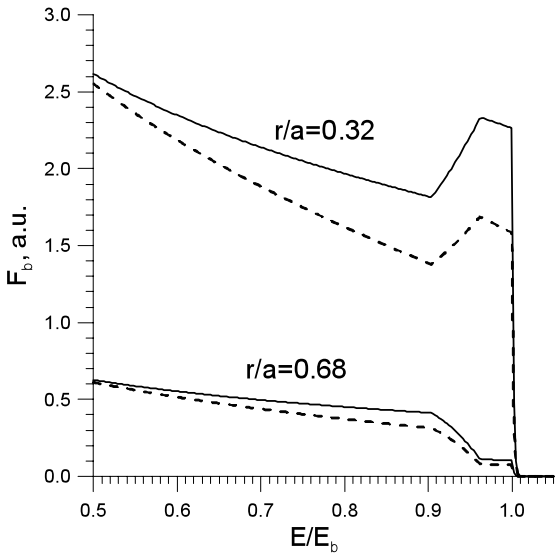

Figure 25. Effect of anomalous radial diffusion on $F_b(E)$. Here $\tilde{D} = 1$ for $0.95 < v/v_b < 0.98$, $\chi_{b1} = 0.6$, $\chi_{b2} = 0.72$, $\delta\chi = 0.2$ and the radial profile of the NBI is $S \propto (1 - r^2/a^2)^6$. Notations are solid line, $\chi = 0.73$ and dashed line, $\delta\chi = 0.81$.

The matter is that the particles observed by the NPA at $R = 78$ cm have orbits that traverse the periphery region. This follows from figures 26(*a*) and (*b*) where orbits of the NPA-observed 90 keV particles and particles reaching the limiter are shown. As seen from figure 26(*a*), the maximum major radius, R, on the particle orbit with $\chi \sim 0.7$ is $R = 135$ cm. This implies that the average flux surface radial coordinate, r, of this orbit is $r = (135 - 78)/2 = 28.5$ cm. On the other hand, figure 26(*b*) shows the orbit intersects the limiter ($R = 155$ cm) after taking into account that the Larmor radius ($v\sqrt{1-\chi^2}/\omega_B$) of a 90 keV particle with a pitch of $0.7 - 0.8$ is about 10 cm. The average flux surface radial coordinate of this orbit is $r = (145 - 60)/2 = 42.5$ cm. This is actually the effective plasma radius, a_{eff}, in the sense that particles with a larger average radius are lost. Now we see that r/a_{eff} for the orbit observed by the NPA is $r/a_{eff} = 28.5/42.5 = 0.67$ which implies that the considered particle is a periphery one.

It follows from figure 25 that spatial diffusion with $\tilde{D}_r \sim 1$ can hardly lead to the observed large HEFs. However, in our calculations we neglected terms with mixed derivatives in equation (4). Because of these terms, the particle velocity diffusion is accompanied by radial diffusion, so that

$$\frac{\Delta r}{\rho} = k_\vartheta \rho \frac{\omega_B}{2\omega}\frac{\Delta E}{E}, \qquad E = E_b \exp\left[-\frac{\omega}{l\omega_B}(\chi^2 - \chi_b^2)\right], \tag{13}$$

where $\rho = v/\omega_B$ and $\Delta E = E_b - E$. For instance, when $\Delta E/E \sim 0.1, l = 1$ and a particle is displaced by $\Delta r \sim 10$ cm we obtain from equation (13) that the particle pitch angle changes by $\Delta\chi \sim 0.2$ provided $f \sim 700$–1000 kHz and $k_\vartheta\rho = 3 - 4$. This estimate and figure 26 show that particles observed by the NPA ($R = 78$ cm, $\chi \sim 0.7$) can reach the limiter and be lost. Due to the fact that the characteristics of $\hat{\Pi}$ in velocity space at $l = 1$, $\omega_B/\omega \gg 1$ are close to $v = \text{const}$, we can model this mechanism by equation (1) with an artificially large pitch-angle scattering parameter α under the assumption that $D_r = 0$ and that particles are lost at a certain pitch angle due to pitch-angle diffusion. The results of calculations are shown in figure 27. We observe that a HEF with $H \approx 7$ is formed that corresponds, for example, to the HEF in NSTX discharge SN132800. Note that because the particles move along the characteristics determined by equation (13), even a very large radial diffusion coefficient ($\tilde{D}_r \gg 1$) does not lead to the escape of particles from the core region to the wall.

When choosing the sink of the particles at $\chi > \chi_b$, we took into account the following. The velocity anisotropy of F_b is a destabilizing factor when the contribution of the region with $\partial F_b/\partial\chi < 0$ dominates in the expression for the growth rate. It is likely that this was the case for HF waves because only particles with sufficiently large χ can interact with the energetic ions through the cyclotron resonance. Taking this into account, we assume that particles escape from the plasma at a certain pitch angle exceeding the injection pitch angle.

Let us see whether the condition $\tilde{D}_\chi \gg 1$ can be satisfied. Using an explicit form of D given in [56] along with equations (7) and (8), in the case of the $l = 1$ resonance we obtain the following estimate:

$$\tilde{D}_\chi = \pi\omega\tau_s^e(\chi^{-2} - 1)\left(\frac{L_n}{2\rho}\frac{\omega_B}{\omega}\frac{\tilde{n}_e}{n_e}\right)^2 \tag{14}$$

where $L_n = |\mathrm{d}\ln n_e/\mathrm{d}r|^{-1}$. We find that the magnitude $\tilde{D}_\chi \sim 5$ used in our calculation (for which $\tilde{D}_r \sim 1$ at $k_\vartheta\rho \sim 3$) is quite reasonable when $\delta n_e/n_e \sim 2\times10^{-4}$ in the instability region, as estimated in section 4.

In conclusion, we have shown that pitch-angle scattering caused by Coulomb collisions makes the dependence of F_b on E at the pitch angle of injection much weaker than $E^{-3/2}$. This facilitates the formation of a HEF by plasma instabilities driven by the energetic ions. It is found that these instabilities affect F_b in various ways. However, most of mechanisms lead to small HEFs with $H = F_{max}/F_{min} \sim 1$ whereas

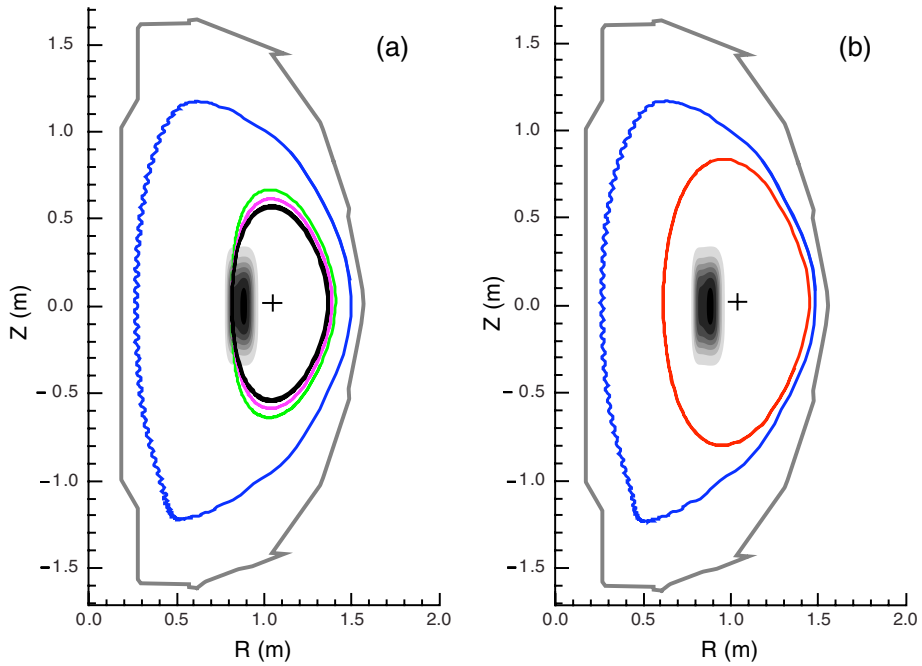

Figure 26. Particle orbits calculated with the code ORBIT for NSTX discharge SN132800 at the moment $t = 0.5$ s (when the HEF was produced). Panel (a): orbits of 90 keV particles having different pitch angles at the point $R = 78$ cm, $\vartheta = \pi$ (i.e. in the inboard equatorial plane); the orbit closest to the edge has $\chi = 0.1$ and the farthest one has $\chi = 0.9$. Panel (b): the outermost confined orbit with $\chi = 0.7$ in the inboard equatorial plane. It follows from here that the particles with Larmor radii $\rho \sim 10$ cm can reach the limiter ($R = 155$ cm) from the point $R = 78$ cm, $\vartheta = \pi$ if they are displaced by $\Delta r = 10$ cm. The shaded rectangle depicts the footprint of the beam primary neutrals (i.e. excluding halo neutrals).

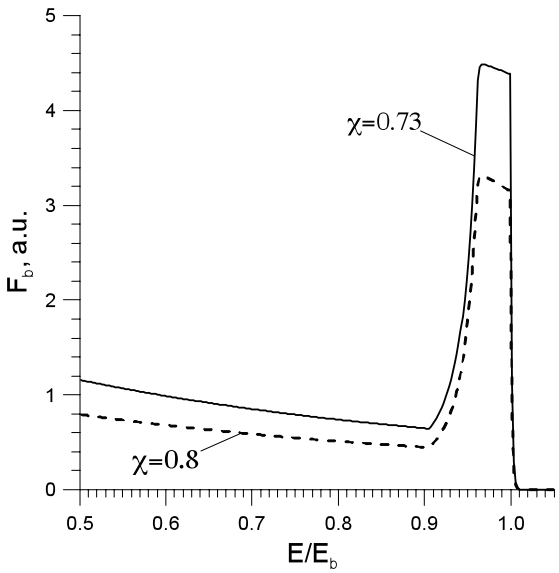

Figure 27. Modelling of QL $F_b(E)$-distortion accompanied by particle loss in NSTX. The particles are lost at $\chi = 0.9$, the anomalous diffusion coefficient is $\tilde{D}_\chi = 9.5(1 - \chi^2)$ for $0.95 < v/v_b < 0.98$ and the injection profile parameters are $\chi_{b1} = 0.6$, $\chi_{b2} = 0.72$ and $\delta\chi = 0.2$.

$H \gg 1$ was observed in many NSTX experiments. The only mechanism that was found to lead to large H in NSTX is the QL evolution of $F_b(E, \chi, r)$ in phase space and the concomitant loss of some particles that occurs due to interaction through cyclotron resonance of the particles with destabilized modes having sufficiently high frequencies, $f \sim$ 700–1000 kHz, in the plasma frame. The calculated wave amplitudes required for this QL distortion of $F_b(E, \chi, r)$ are quite reasonable.

8. Discussion and summary

A phenomenon bearing similarities to the HEF observed on NSTX has been reported for NPA energetic-ion spectra measured on START [59] in discharges heated using 30 keV hydrogen NBI. Termed a 'bump-on-tail', the START spectra exhibit a variation with energy that is significantly more gradual compared with the 'spike-on-tail' characteristic of the HEF in NSTX. Although energetic particle-driven instabilities are invoked as a contributing mechanism on START, a significant role is also attributed to orbit excursions into a large volume well beyond the separatrix. Combined with the high neutral density enveloping the plasma, this can result in a depletion of the energetic-ion population during the slowing-down process leaving the noted 'bump-on-tail' in the full energy region of the spectrum. Highly structured NPA spectra were also observed in MAST [26] during H-mode discharges that under some conditions are likewise attributed to large orbit radial excursions outside the plasma separatrix. Such orbit excursion effects do not play a significant role in NSTX because of the small volume between the separatrix and the vacuum vessel internal structures compared with START and MAST. Other than the above, a literature search did not reveal any report of phenomena on other magnetic fusion devices that were comparable to the HEF observed on NSTX.

For charge exchange neutral particle measurements on NSTX, quantifying the relative weighting between core (beam primary and halo) and edge emissivity contributions can be

challenging. In the core, the emissivity is driven primarily by the elected NB injection scenario and the density profile that affect attenuation of both the input beam and the emerging charge exchange flux. The edge is more complex being affected by factors such as discharge scenarios (e.g. L-mode versus H-mode), spatially distributed gas puffing, vacuum vessel conditioning (e.g. lithium deposition on plasma-facing components for edge density and recycling control) and ELM activity of multiple types. For the highly energetic-ion characteristic of the HEF, the situation is complicated even further by spatially extended ion orbits that traverse both the plasma core and peripheral regions as noted earlier in figure 26. To make matters worse, the edge neutral density is poorly diagnosed on NSTX. From an experimental standpoint, core emissivity can often be quantified using brief single or multiple beam notches (∼10–20 ms, i.e. short compared with energetic ion slowing-down times). The reduction in NPA flux varies somewhat with the source(s) being notched, but approaches ∼1/3 per source as would be expected. To provide background corrections, NSTX beam-based diagnostics always utilize notches to zero beam power. However, such notching does not work for HEF emissivity localization because the notch simultaneously terminates the HEF. Following the notch, the HEF reemerges with growth times of ∼20–80 ms. From a simulation standpoint, TRANSP calculation of the core charge exchange neutral emissivity is compromised by improper treatment of halo neutrals that are uniformly distributed over the plasma volume rather than properly being constrained to a 'cloud' enveloping the beam footprint. With this caveat, the TRANSP-calculated edge emissivity typically exceeds the core value by an order of magnitude or more. (Note that for the TRANSP calculation in figure 2, the edge emissivity has been excluded by choice of the NPA sightline origin in order to focus on core emission.) As documented by the FIDASIM code [60] that does provide correct treatment of halo neutrals, the halos can approximately double the emissivity in both magnitude and radial width compared with the beam primary neutrals alone. This significantly affects the magnitude of the simulated signal but also (albeit to a modest extent) the shape of the energetic-ion spectrum.

One of the issues in the NSTX database related to the HEF studies was a significant correlation among various discharge variables, most notably between the MHD modes and the NBI heating power and injection energy. It was pointed out earlier that (in addition to certain MHD behaviour) the occurrence of HEFs required existence of a H-mode discharge *and* injected beam power $P_b \geqslant 4$ MW. However, it should be noted that these are not independent conditions. At $P_b \geqslant 4$ MW, NSTX discharges routinely undergo an early L–H transition unless special steps are taken to suppress such a transition (and, moreover, GAE and CAE activity become increasingly robust). Future dedicated scans are needed to elucidate this correlation and determine the parametric dependence on such parameters to a satisfactory degree of certainty. The following conjecture can be offered concerning the MHD behaviour attending occurrence of the HEF: namely, the HEF only appears on the NB-injected energetic-ion spectrum in discharges where NTM or kink-type modes ($f < 50$ kHz) are absent, TAE activity ($f \sim 50$–150 kHz) is weak and GAE activity ($f \sim 400$–1000 kHz) is robust. CAE activity ($f > 1000$ kHz) is usually sporadic or absent during the HEF. Tentatively, assume that the HEF is driven by a resonant GAE wave–particle interaction causing redistribution of the energetic-ion distribution, $F_b(E, v_\parallel/v, r)$. Furthermore, GAE activity is generally core-localized with the other modes arising in a broad region between the core and the plasma periphery. In the presence of the NTM/TAE modes, the GAE-driven modification of the energetic-ion distribution, $F_b(E, v_\parallel/v, r)$, that is observed by the line-integrated NPA measurements could be dominated or masked by this spatially intervening MHD activity. (Or mode coupling could obfuscate the GAE wave–particle resonance.) Thus the HEF is not driven by relaxation of NTM/TAE activity but its observation by the NPA is facilitated by such relaxation.

It is apparent from section 7 that progress has been made in identifying the mechanism of HEF formation: namely, the HEF appears to be caused by a resonant GAE wave–particle interaction that modifies the energetic-ion distribution in physical and phase space. However, understanding the details of the HEF evolution and the interplay of MHD activity attending the occurrence of the HEF points to the need for an appropriate numerical simulation capability. A promising tool for this purpose is the SPIRAL code that imports an initial TRANSP-calculated energetic-ion distribution, $F_b(E, v_\parallel/v, r)$, and evolves this distribution in the presence of background plasma profiles under drive from wave–particle resonances due to GAE or other Alfvén eigenmode structures. The eigenmodes are constructed using the HYM code that provides three-dimensional simulations of energetic-ion-driven instabilities including fully kinetic ion description and nonlinear effects. The SPIRAL code can also treat superposition of multiple modes and thus address the interplay between MHD mode activity and the HEF occurrence as noted above. However, analysis of the physics of the HEF formation using the SPIRAL code remains a work in progress at the present time.

Acknowledgments

This work was supported by the US Department of Energy under Contract No DE-AC02-09CH11466. This work was partly supported by Project #4588 of the Science and Technology Center in Ukraine, US DOE Grant Nos DE-FG02-89ER53296 and DE-SC0001288 (U. Wisconsin-Madison), US DOE Grant No DE-FG02-06ER54867 (UC Irvine), US DOE Grant No DE-FG02-99ER54527 (UCLA) and US DOE Grant No DE-FG02-99ER54518 (UC Davis).

References

[1] Ono M. *et al* 2001 Overview of the initial NSTX experimental results *Nucl. Fusion* **41** 1435
[2] Peng Y.-K.M. and Strickler D.J. 1986 Features of spherical torus plasmas *Nucl. Fusion* **26** 769
[3] Menard J.E. *et al* 2007 Overview of recent physics results from the National Spherical Torus Experiment (NSTX) *Nucl. Fusion* **47** S645
[4] Gates D.A. *et al* 2009 Overview of results from the National Spherical Torus Experiment (NSTX) *Nucl. Fusion* **49** 104016
[5] Kaye S.M. *et al* 2005 Progress towards high performance plasmas in the National Spherical Torus Experiment (NSTX) *Nucl. Fusion* **45** S168–80

[6] Heidbrink W.W., Gorelenkov N.N. and Murakami M. 2002 Beam-driven energetic particle modes in advanced tokamak plasmas *Nucl. Fusion* **42** 972
[7] Fredrickson E.D. *et al* 2003 Wave driven fast ion loss in the National Spherical Torus Experiment *Phys. Plasmas* **10** 2852
[8] Gorelenkov N.N. *et al* 2004 Beam ion driven instabilities in the National Spherical Torus Experiment *Phys. Plasmas* **11** 2586
[9] Fredrickson E.D. *et al* 2006 Fast ion loss in a 'Sea-of-TAE' *Nucl. Fusion* **47** S926–S93
[10] Fredrickson E.D. *et al* 2009 Modeling fast-ion transport during toroidal Alfven eigenmode avalanches in National Spherical Torus Experiment *Phys. Plasmas* **16** 122505
[11] Podestà M. *et al* 2009 Experimental studies on fast-ion transport by Alfvén wave avalanches on the National Spherical Torus Experiment *Phys. Plasmas* **16** 056104
[12] Darrow D.S. 2008 MHD induced neutral beam ion loss from NSTX plasmas *Nucl. Fusion* **48** 084004
[13] Medley S.S. *et al* 2004 MHD-induced energetic ion loss during h-mode discharges in the National Spherical Torus Experiment *Nucl. Fusion* **44** 1158
[14] Menard J.E. *et al* 2006 Observation of instability-induced current redistribution in a Spherical Torus Plasma *Phys. Rev. Lett.* **97** 095022
[15] Garcia-Munoz M. *et al* 2007 NTM induced fast-ion losses in ASDEX Upgrade *Nucl. Fusion* **47** L10
[16] Garcia-Munoz M. *et al* 2009 MHD induced fast-ion losses on ASDEX Upgrade *Nucl. Fusion* **49** 085014
[17] Medley S.S., Darrow D.S., Liu D. and Roquemore A.L. 2005 Prompt loss of energetic ions during early neutral beam injection in the National Spherical Torus Experiment *Princeton Plasma Physics Laboratory Report* PPPL-4060
[18] Jarvis O.N., van Belle P., Sadler G., Whitfield G.A.H., Cecil F.E., Darrow D. and Esposito B. 2001 Measurements of escaping fast particles using a thin-foil charge collector *Fusion Sci. Technol.* **39** 84
[19] Darrow D.S. 2008 Scintillator based energetic ion loss diagnostic for the National Spherical Torus Experiment *Rev. Sci. Instrum.* **79** 023502
[20] Fredrickson E.D., Chen L. and White R.B. 2003 Bounce precession fishbones in the National Spherical Torus Experiment *Nucl. Fusion* **43** 1258
[21] Crocker N.A. *et al* 2008 Alfvén cascade modes at high β in the National Spherical Torus Experiment *Phys. Plasmas* **15** 102502
[22] Fredrickson E.D. *et al* 2006 Collective fast ion instability-induced losses in National Spherical Torus Experiment *Phys. Plasmas* **13** 056109
[23] Podestà M. *et al* 2011 Non-linear dynamics of toroidicity-induced Alfvén eigenmodes on the National Spherical Torus Experiment *Nucl. Fusion* **51** 063035
[24] Akers R.J. *et al* 2002 Neutral beam heating in the START spherical tokamak *Nucl. Fusion* **42** 122
[25] Akers R.J. *et al* 2003 Transport and confinement in the Mega Ampere Spherical Tokamak (MAST) plasma *Plasma Phys. Control. Fusion* **45** A175
[26] Tournianski M.R. *et al* 2005 Anisotropic fast neutral spectra in the MAST spherical tokamak *Plasma Phys. Control. Fusion* **47** 671
[27] Heidbrink W.W. *et al* 2003 The confinement of dilute populations of beam ions in the National Spherical Torus Experiment *Nucl. Fusion* **43** 883
[28] Medley S.S. *et al* 2007 Status of recent experimental and analytical investigation of MHD-induced energetic ion redistribution or loss in the National Spherical Torus Experiment *Princeton Plasma Physics Laboratory Report* PPPL-4235
[29] Medley S.S. *et al* 2007 Neutral particle analyzer vertically scanning measurements of MHD-induced energetic ion redistribution or loss in the National Spherical Torus Experiment *Princeton Plasma Physics Laboratory Report* PPPL-4270
[30] Smith D.R., Feder H., Feder R., Fonck R.J., Labik G., McKee G.R., Schoenbeck N., Stratton B.C., Uzun-Kaymak I. and Winz G. 2010 Overview of the beam emission spectroscopy diagnostic system on the National Spherical Torus Experiment *Rev. Sci. Instrum.* **81** 10D717
[31] Crocker N.A., Peebles W.A., Kubota S., Zhang J., Fredrickson E.D. and LeBlanc B.P. 2011 High spatial sampling global structure measurements via multichannel reflectometry in NSTX *Plasma Phys. Control. Fusion* **53** 105001
[32] Smith D.R., Mazzucato E., Lee W., Park H.K., Domier C.W. and Luhmann N.C. Jr 2008 A collective scattering system for measuring electron gyroscale fluctuations on the National Spherical Torus Experiment *Rev. Sci. Instrum.* **79** 123501
[33] Juhn J.-W., Lee K.C., Hwang Y.S., Domier C.W., Luhmann N.C. Jr, LeBlanc B.P., Mueller D., Gates D.A. and Kaita R. 2010 Fringe-jump corrected far infrared tangential interferometer/polarimeter for real-time density feedback control system of NSTX plasmas *Rev. Sci. Instrum.* **81** 10D540
[34] Delgado-Aparicio L.F. *et al* 2007 A 'multi-colour' SXR diagnostic for time and space-resolved measurements of electron temperature, MHD activity and particle transport in MCF plasmas *Plasma Phys. Control. Fusion* **49** 1245
[35] Medley S.S. *et al* 2008 Invited review article: Contemporary instrumentation and application of charge exchange neutral particle diagnostics in magnetic fusion energy experiments *Rev. Sci. Instrum.* **79** 011101
[36] Medley S.S. and Roquemore A.L. 2004 Neutral particle analyzer diagnostic on in the National Spherical Torus Experiment *Rev. Sci. Instrum.* **75** 3625
[37] Medley S.S. and Roquemore A.L. 1998 Construction and operation of parallel electric and magnetic field spectrometers for mass/energy resolved multi-ion charge exchange diagnostics on the Tokamak Fusion Test Reactor *Rev. Sci. Instrum.* **69** 2651
[38] Medley S.S., Gorelenkov N.N., Bell R.E., Fredrickson E.D., Gerhardt S.P., LeBlanc B.P., Podestà M., Roquemore A.L. and the NSTX Team 2010 Transient enhancement ('spike-on-tail') observed on neutral-beam-injected energetic ion spectra using the $E \| B$ neutral particle analyzer in the National Spherical Torus Experiment *Princeton Plasma Physics Laboratory Report* PPPL-4528
[39] LeBlanc B.P., Bell R.E., Johnson D.W., Hoffman D.E., Long D.C. and Palladino R.W. 2003 Operation of the NSTX Thomson scattering system *Rev. Sci. Instrum.* **74** 1659
[40] Bell R.E. and Feder R. 2010 Measurement of poloidal velocity on the National Spherical Torus Experiment (invited) *Rev. Sci. Instrum.* **81** 10D724
[41] Smith D.R. 2011 private communication, University of Madison-Wisconsin
[42] White R.B., Gorelenkov N., Heidbrink W.W. and Van Zeeland M.A. 2010 Particle distribution modification by low amplitude modes *Plasma Phys. Control. Fusion* **52** 045012
[43] Stutman D., Delgado Aparicio L., Gorelenkov N., Finkenthal M., Fredrickson E., Kaye S., Mazzucato E. and Tritz K. 2009 Correlation between electron transport and shear Alfvén activity in the National Spherical Torus Experiment *Phys. Rev. Lett.* **102** 115002
[44] Gorelenkov N.N., Fredrickson E., Belova E., Cheng C.Z., Gates D., Kaye S. and White R. 2003 Theory and observations of high frequency Alfvén eigenmodes in low aspect ratio plasmas *Nucl. Fusion* **43** 228
[45] Podestà M., Heidbrink W.W., Bell R.E. and Feder R. 2008 The NSTX fast-ion D-alpha diagnostic 2008 *Rev. Sci. Instrum.* **79** 10E521

[46] Heidbrink W.W. 2010 Fast-ion D_α measurements of the fast-ion distribution (invited) 2010 *Rev. Sci. Instrum.* **81** 10D727
[47] Liu D. *et al* 2010 Profiles of fast ions that are accelerated by high harmonic fast waves in the National Spherical Torus Experiment *Plasma Phys. Control. Fusion* **52** 025006
[48] Kugel H.W. *et al* 2008 The Effect of lithium surface coatings on plasma performance in the National Spherical Torus Experiment *Phys. Plasmas* **15** 056118
[49] Bell M.G. *et al* 2009 Plasma response to lithium-coated plasma-facing components in the National Spherical Torus Experiment *Plasma Phys. Control. Fusion* **51** 124054
[50] Mansfield D.K. *et al* 2010 A simple apparatus for the injection of lithium aerosol into the scrape-off layer of fusion research devices *Fusion Eng. Des.* **85** 890
[51] Goldston R.J., McCune D.C., Towner H.H., Davis S. L., Hawryluk R.J. and Schmidt G.L. 1981 New techniques for calculating heat and particle source rates due to neutral beam injection in axisymmetric tokamaks *J. Comput. Phys.* **43** 61
[52] Onega J., Evrard M. and McCune D. 1998 Numerical transport codes *Trans. Fusion Technol.* **33** 182
[53] Kaye S.M. *et al* 2007 Confinement and local transport in the National Spherical Torus Experiment (NSTX) *Nucl. Fusion* **47** 499
[54] Gerhardt S.P. *et al* 2011 Calculation of the non-inductive current profile in high-performance NSTX plasmas *Nucl. Fusion* **51** 033004
[55] Kolesnichenko Ya.I., Parail V.V. and Pereverzev G.V. 1992 *Reviews of Plasma Physics* vol 17 (New York: Consultant Bureau) pp 1–192
[56] Belikov V.S. and Kolesnichenko Ya.I. 1982 Derivation of the quasi-linear theory equations for the axisymmetric toroidal systems *Plasma Phys.* **24** 61
[57] Kolesnichenko Ya.I., White R.B. and Yakovenko Yu.V. 2006 High frequency shear Alfvén instability driven by circulating energetic ions in NSTX *Phys. Plasmas* **13** 122503
[58] Tsuji H., Katsurai M., Sekiguchi T. and Nakano N. 1976 Time-dependent solution of Fokker–Planck equation for alpha-particles and its effect on alpha-particle heating characteristics in a D–T fusion reactor *Nucl. Fusion* **16** 287
[59] McClements K.G. *et al* 1999 Physics of energetic particle-driven instabilities in the START spherical tokamak *Plasma Phys. Control. Fusion* **41** 661
[60] Heidbrink W.W., Liu D., Luo Y., Ruskov E. and Geiger B. 2011 A code that simulates fast-ion D_α and neutral particle measurements *Commun. Comput. Phys.* **10** 716